First-principles theory for Earth's tropical-midlatitude climate boundary

Tsubasa Kohyama*, Hiroaki Miura, and Kazuya Yamazaki

Department of Information Sciences, Ochanomizu University, Tokyo, Japan

Department of Earth and Planetary Science, The University of Tokyo, Tokyo, Japan

Information Technology Center, The University of Tokyo, Chiba, Japan

*Corresponding author address: Department of Information Sciences, Ochanomizu University, 2-1-1, Bunkyo-ku, Tokyo, Japan, 112-8610

E-mail: tsubasa@is.ocha.ac.jp

ABSTRACT

In Earth's climate, the boundary between the tropics and midlatitudes is a key determinant of temperature and precipitation characteristics[1], influencing human societies through daily weather[2,3], atmospheric chemistry[4], carbon cycling[5], and vegetation distribution[6,7]. The physical origin of these climate zones has been investigated through idealized simulations[8–14], observations[15,16], and state-of-the-art climate models[17–20]. However, a first-principles theory to explain the boundary position remains largely unexplored. Here we propose a theory to understand this climate bifurcation through a thermal-mechanical decomposition using the first law of thermodynamics. We introduce a dimensionless parameter, the thermal-mechanical ratio ($\mathscr{T}/\mathscr{M}$), to quantify thermal and mechanical contributions to vertical motion. This parameter offers a first-principles definition of "tropicalness": regions where thermal contribution dominates are tropical ($\mathscr{T}/\mathscr{M} \gtrsim 10$), whereas regions with non-negligible mechanical contributions are midlatitudinal ($\mathscr{T}/\mathscr{M} \lesssim 10$). We derive a simple model to describe the determination mechanism of the boundary position from fundamental physical constants, which explains observed seasonality, global warming response, and the El Niño-Southern Oscillation sensitivity. This framework provides robust theoretical foundations for understanding anthropogenic tropical expansion[21,22], informing climate change adaptation strategies[23]. Applications to other planetary atmospheres are also suggested[24,25].

Introduction

Earth contains distinct tropical and midlatitude climate zones. The tropics maintain warm, humid conditions throughout the year with vigorous convective rainfall as the dominant precipitation mechanism. By contrast, the midlatitudes exhibit pronounced seasonality, with frontal cyclones as the primary precipitation source. The boundary between the tropics and the midlatitudes determines a wide range of climate elements, such as temperature distribution[1,3], the genesis and decay regions of tropical cyclones[26], precipitation patterns[2,27], and atmospheric chemistry[4]. This climate boundary governs the climate of regions where approximately half the global population resides[22], in addition to defining vegetation and ecosystem[28,29], exerting diverse influences on the entire Earth's system.

The fundamental difference between these two climate zones stems from the latitude-dependent relative importance of solar heating and Earth's rotation. In the tropics, heating dominates over rotational effects, so vertical convective motion driven by local heating plays a paramount role. In the midlatitudes, rotation dominates, making the relaxation of meridional temperature gradients the primary driving source. Similar physical mechanisms also appear in other planetary atmospheres such as the Martian atmosphere[24,25], indicating universal features of planetary atmospheres.

Research over the past decades includes idealized simulations[8–14], phenomenological descriptions[15,16], and global climate model experiments[17–20] to understand the tropical-midlatitude (T/M) boundary latitude, yielding valuable theoretical insights. Despite these excellent contributions, however, incorporating complex atmospheric behaviors (e.g., atmospheric stability, moist processes, and eddy effects) into first-principles explanations remains difficult. Currently, quantitative predictions of boundary fluctuations and future changes rely on phenomenon-specific physical arguments that depend heavily on observational data and/or model assumptions.

As an implication for social impacts, a poleward shift of the T/M boundary, which is referred to as the "tropical expansion", is believed to cause discontinuous climate changes across wide regions on Earth[15,21]. This expansion threatens local agriculture and water resources, which makes societal infrastructure reconstruction inevitable in the near future[23]. However, numerous studies employ a large variety of phenomenological bases to project the expansion, leaving no consensus on quantitative estimates such as warming-induced expansion rates[22].

These circumstances demand a unified understanding of the T/M boundary behavior based on first principles. Hence, this study proposes a theory to understand what bifurcates the tropics and the midlatitudes. Based on physically robust minimal assumptions, this framework explains the boundary position climatology, seasonal variability, global warming responses, and interannual variations. Our theory deepens understanding of Earth's climate, as well as providing new perspectives for adjacent fields including ecosystem distributions and other planetary atmospheres.

The T/M theory

The first law of thermodynamics for a unit mass of air reads:

$$-\alpha\omega = j - c_{\mathrm{p}}\frac{DT}{Dt} \tag{1}$$

where α is specific volume (inverse density), ω is pressure change rate (equivalent to vertical motion under hydrostatic balance, with $\omega < 0$ for upward motion), j is diabatic heating rate, c_{p} is specific heat at constant pressure, and DT/Dt is temperature tendency. Throughout this paper, we consider equation (1) in the context of large-scale atmospheric dynamics, interpreting each term as a coarse-grained quantity, rather than applying it to individual convective systems or small-scale motions.

Under hydrostatic balance, the equation (1) can be interpreted as a decomposition of vertical motion into thermally- and mechanically-determined components. Therefore, we hereafter call the first term of the right-hand side the "thermal source" and the second term the "mechanical source". These two sources are physically distinct. The thermal source j drives vertical motion by acting on the thermodynamic state within the air parcel through molecular-scale processes, such as radiation and surface heat flux, without necessarily requiring air temperature changes. By contrast, the mechanical source $-c_{\mathrm{p}}DT/Dt$ constrains vertical motion through adiabatic adjustment to large-scale dynamic conditions outside the air parcel, manifesting as an air temperature change as a macroscopic property of the molecular ensemble.

We note that the term "thermal/mechanical source" here follows the enthalpy representation of the first law of thermodynamics (*see* Supplementary Text 1), and should not be confused with the meteorological convention. For example, thermal advection, which is realized by mechanics rather than heat, belongs to the mechanical source in our framework. Critically, atmospheric circulation structure and response characteristics differ fundamentally depending on which source, as defined in this particular framework, balances vertical motion.

Here we propose to define the tropics as regions where the thermal source dominates over the mechanical source, and the midlatitudes as regions where the mechanical source remains significant. Therefore, we introduce a dimensionless parameter to characterize the relative importance of these two sources, the thermal-mechanical ratio (T/M ratio):

$$\mathscr{T}/\mathscr{M} := \left| \frac{[\, j \,]}{[\, -c_{\mathrm{p}}DT/Dt \,]} \right| \simeq \left| \frac{[\, j \,]}{gDZ_{\mathrm{T}}/Dt} \right| \sim \frac{J}{fU^2} \cdot \frac{L^2}{L_{\mathrm{R}}^2} \tag{2}$$

where $[\,]$ denotes mass-weighted vertical average over the troposphere, g is gravitational acceleration, Z_{T} is tropopause height, J is the scale of diabatic heating per unit mass, f is the magnitude of the Coriolis parameter, U is typical wind speed scale, L is typical horizontal scale, and L_{R} is the

Rossby deformation radius. The symbols $\simeq$ and $\sim$ in equation (2) hold under hydrostatic balance and quasi-geostrophic balance assumptions, respectively (*see* Methods), which provides a widely applicable scaling for large-scale atmospheric motion. In particular, here we assume that the atmosphere consists of a troposphere and a stratosphere with distinct lapse rates, which allows us to approximate the tropospheric vertical-mean temperature using Z_{T}.

In the coarse-grained large-scale atmospheric dynamics, the thermal and mechanical sources consists of the following physical processes. The thermal source $\mathscr{T} \sim J$ represents the rate of energy conversion from diabatic heating to kinetic energy. This thermal conversion rate is primarily determined by the difference between incoming solar and outgoing thermal radiation (though incoming radiation may first warm the surface before injection as sensible or latent heat; J includes all net diabatic heating). Conversely, the mechanical source $\mathscr{M} \sim fU^2 L_{\mathrm{R}}^2/L^2$ represents the rate of conversion from available potential energy to kinetic energy (baroclinic energy conversion). This mechanical conversion rate is determined primarily by Earth's rotation rate and atmospheric flow state.

As the simplest treatment of the T/M ratio, we could consider its large and small limits. The former represents thermally-dominated tropical dynamics, whereas the latter represents mechanically-dominated midlatitude dynamics. Indeed, taking $\mathscr{T}/\mathscr{M} \to \infty$ in the atmospheric basic equations yields the well-known governing equations for the tropics (Weak Temperature Gradient (WTG) system)[30], whereas taking $\mathscr{T}/\mathscr{M} \to 0$ yields those of midlatitudes (Quasi-geostrophic potential vorticity conservation system)[31] (Supplementary Text 2).

Next, to define the tropical and midlatitude regions objectively, we set the criterion for negligibility at one-tenth. With this choice, regions with $\mathscr{T}/\mathscr{M} \gtrsim 10$ follow tropical dynamics, whereas regions with $\mathscr{T}/\mathscr{M} \lesssim 10$ follow midlatitude dynamics. The choice of 10 rather than unity as the critical value is based on the asymmetric role of the thermal and mechanical sources. That

is, the tropics are characterized by thermal source dominance with negligible mechanical source, whereas the midlatitudes require both sources to be significant.

To discuss the transition zone between the tropical and midlatitude extremes, we must choose the horizontal scale appropriately for coarse-graining. When horizontal scales are too small, convection and individual disturbances are not spatially averaged, so we cannot consider the large-scale dynamical structure that defines the boundary. Conversely, when horizontal scales are too large, spatial averaging through coarse-graining encompasses both tropical and midlatitude characteristics, losing the ability to resolve the climate regime bifurcation. Therefore, to balance these considerations, we choose a typical horizontal scale of large-scale fields to satisfy $L^2 \sim 10L_{\mathrm{R}}^2$.

The "T/M boundary layer", where $\mathscr{T}/\mathscr{M} \sim 10$, smoothly connects the two interior regions governed by different atmospheric dynamics. The condition for the T/M boundary layer obtained from the above coarse-graining, considering the scaling in equation (2), simplifies to:

$$\mathscr{T} \sim 10\mathscr{M} \quad AND \quad L^2 \sim 10L_{\mathrm{R}}^2 \quad \Longrightarrow \quad J \sim fU^2 \tag{3}$$

This relation becomes crucial when constructing the conceptual model in the next section, which provides an a priori expectation that the transition zone must occupy a narrow band of latitude at a particular latitude.

Under the above coarse-graining, $\mathscr{T}/\mathscr{M}$ varies over Earth with orders ranging from 10^{-1} to 10^3. Therefore, when analyzing spatiotemporal variations of $\mathscr{T}/\mathscr{M}$, it is convenient to examine climatology, deviations, and trends of $\log_{10}(\mathscr{T}/\mathscr{M})$. For climatological means (denoted by overline), the approximation $\overline{\log_{10}(\mathscr{T}/\mathscr{M})} \simeq \log_{10}(\overline{\mathscr{T}}/\overline{\mathscr{M}})$ generally holds with good precision, but we must note that $\overline{\log_{10}(\mathscr{T}/\mathscr{M})} \neq \log_{10}\overline{(\mathscr{T}/\mathscr{M})}$.

Theoretical prediction and observational validation of the T/M boundary latitude

Annual climatology of the T/M boundary

The T/M boundary is where the orders of thermal and mechanical sources intersect. To understand the determination mechanism of the T/M boundary latitude from first principles, we consider the static model shown in Fig. 1. Mathematical and physical details appear in Methods, summarized below.

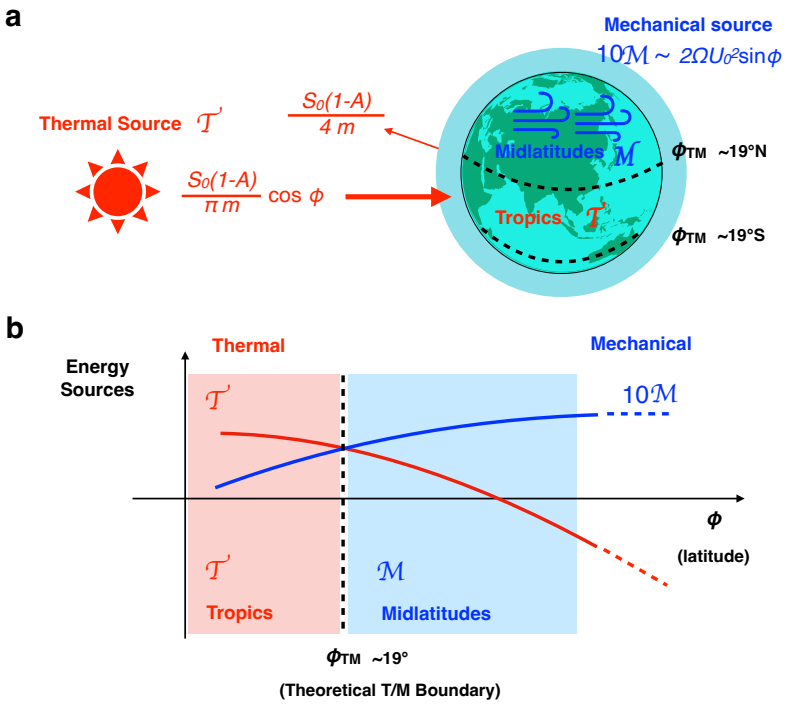

FIG. 1. **Theoretical framework of the Thermal-Mechanical (T/M) theory showing the relationship between enthalpy sources and climate regimes. a**, Conceptual model considered in this study. **b**, The diagram illustrates how the ratio of thermal ($\mathscr{T}$) to mechanical ($\mathscr{M}$) energy sources determines the boundary between tropical and midlatitude dynamics.

First, the scale $\mathscr{T} \sim J$ of the thermal source becomes a monotonically decreasing function of latitude ϕ, due to the local energy imbalance between incoming solar radiation and outgoing thermal

radiation. Here, we represent outgoing radiation by its global-mean value, assuming that atmospheric and oceanic circulation adjust this energy imbalance faster than the climatic timescale. Conversely, the scale of the mechanical source $10\mathscr{M} \sim fU^2$ becomes a monotonically increasing function of ϕ in the latitude bands of interest, since Coriolis force increases from equator to pole with the sine of latitude.

Based on equation (3), the T/M boundary latitude ϕ_{TM} is obtained as the solution to $J(\phi) = f(\phi)U(\phi)^2$, namely:

$$\frac{S_0(1-A)}{\pi m}\cos\phi - \frac{S_0(1-A)}{4m} = (2\Omega\sin\phi)(U(\phi))^2 \tag{4}$$

where S_0 is the solar constant, A is Earth's albedo, π is the mathematical constant, m is the vertically-integrated atmospheric mass per unit area, and Ω is Earth's angular velocity. As a zeroth-order approximation, we treat A and m as global constants. In this study, we hereafter use $S_0 = 1{,}366$ W/m^2, $A = 0.3$, $m = 10{,}327$ kg/m^2, and $\Omega = 7.27 \times 10^{-5}$ /s.

Now, by defining $U_0 := U(\phi_{\mathrm{TM}})$ as the input parameter representing the typical wind speed at the T/M boundary, the first-principles model given by equation (4) yields an analytical solution:

$$\phi = \phi_{\mathrm{TM}}(U_0) := \arctan\left(\frac{S_0(1-A)}{2\Omega U_0^2 \pi m}\right) - \arcsin\left(\frac{S_0(1-A)}{4m\sqrt{4\Omega^2 U_0^4 + S_0^2(1-A)^2/\pi^2 m^2}}\right) \tag{5}$$

For example, by adopting U_0 = 10 m/s as a representative tropospheric wind-scale parameter, the model yields $\phi_{\mathrm{TM}} \simeq 19.0^\circ$, which serves as a first-order estimate of the T/M boundary latitude as validated below.

Atmospheric behavior fundamentally differs between the tropical and midlatitudinal sides of the T/M boundary. The above theoretical value can be validated in detail using reanalysis data, which is obtained by assimilating observations into weather prediction models. Figures 2a and 2b show the 500 hPa geopotential height visualized using "virtual lighting" (*see* Methods), and annual climatology of $\log_{10}(\mathscr{T}/\mathscr{M})$, respectively. The 500 hPa height field suggests that small-

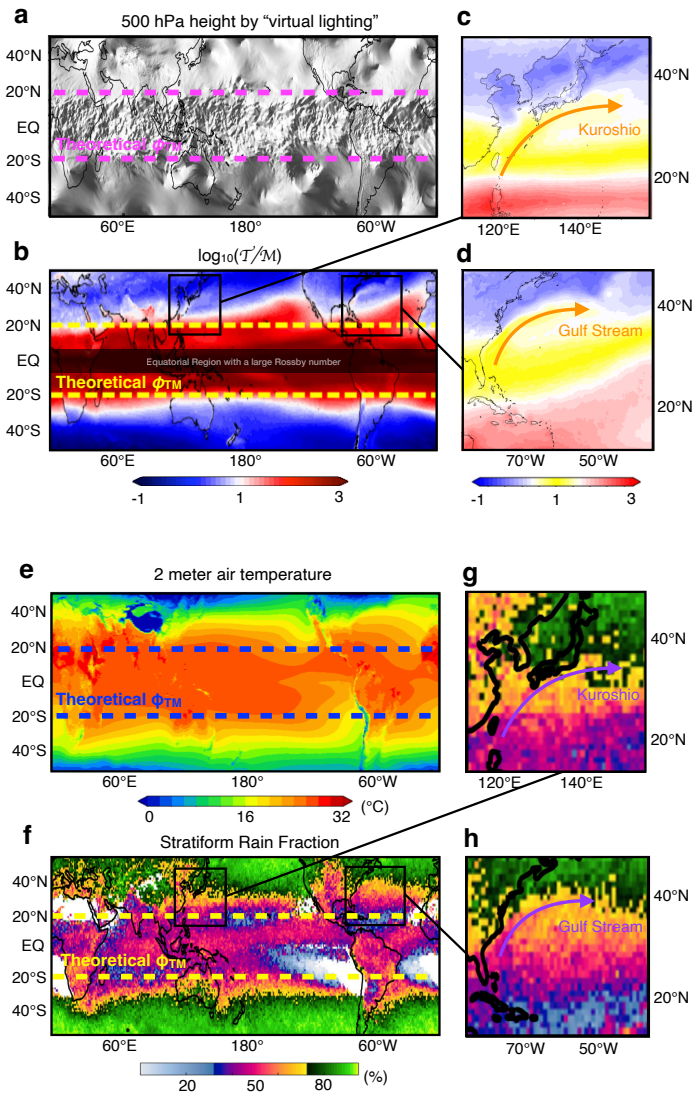

FIG. 2. **Observational validation of the T/M theory and its implications for air temperatures and rainfall.** (a) 500 hPa geopotential height visualization using "virtual lighting" (3:00 Universal Time Coordinated (UTC) on April 20, 2024). (b) Annual climatology of $\log_{10}(\mathscr{T}/\mathscr{M})$. The equatorial region is masked because the scaling in Eqn. (2) is not valid. (c,d) As in (b), but for the Kuroshio and the Gulf Stream regions indicated by the black boxes in (b). (e) Annual climatology of 2-meter air temperature. (f) Annual climatology of stratiform rain fraction by Schumacher and Funk (2023)[27]. (g, h) As in (f), but for the Kuroshio and the Gulf Stream regions. The dashed lines in (a), (b), (e), and (f) represent the theoretical T/M boundary of $\phi_{\mathrm{TM}} = \pm 19.0^{\circ}$. Also shown as solid arrows in (c), (d), (g), and (h) are the approximate positions of the major ocean warm currents.

scale disturbances dominate in the tropics, whereas large-scale pressure gradients dominate in the midlatitudes. This contrast is overall consistent with the $\log_{10}(\mathscr{T}/\mathscr{M})$ distribution, which shows that local heating (large-scale pressure adjustment) balances vertical motion in the tropics (midlatitudes). The zonal-mean T/M boundary latitude calculated from the reanalysis $\mathscr{T}/\mathscr{M}$ distribution (1982-2024 average) is located around 27°. The $\sim 8°$ difference between the simple model and observations is a reasonable discrepancy, attributable to the simplicity of the zeroth-order model, including the choice of the model input U_0 = 10 m/s and the neglect of approximately one-tenth of meridional heat transport by both oceanic and atmospheric dynamics.

The T/M boundary is a crucial demarcation that characterizes Earth's climate system. Figure 2e shows annual-mean 2-meter air temperature. Only equatorward of the T/M boundary, spatial temperature variations are small (i.e., isotherms are nearly absent). Figure 2f shows stratiform rainfall fraction derived by Schumacher and Funk (2023)[27], with the T/M boundary positioned near the 50% contours. Convective rainfall dominates tropical regions, whereas stratiform rainfall increases sharply toward the midlatitudes. This contrast confirms the T/M theory's implications, i.e., the tropics are dominated by vertical mixing with local, thermally-driven convection (e.g., cumulonimbus), whereas the midlatitudes are dominated by the large-scale systems to relax the global, meridional density gradients (e.g., extratropical cyclones). In addition, pressure, humidity, potential vorticity, and convective indices exhibit similar contrasts between climate zones (Supplementary Fig. 3).

At the T/M boundary, mechanical source contribution gradually increases toward the poles, creating a "phase transition" from tropical to midlatitude dynamics. Indeed, the "T/M boundary layer" forms near $T/M \sim 10$ (Fig. 2b, white), where singular behavior emerges due to the coexistence of both tropical and midlatitude characteristics. Furthermore, at the continental east coasts, strong heating from oceanic warm currents lets the T/M boundary layer intrude into the midlat-

itudes ("tropical spillover"). Figures 2c and 2d show $\log_{10}(\mathscr{T}/\mathscr{M})$ distribution in the Kuroshio and Gulf Stream regions, respectively ("T/M boundary layer" highlighted yellow), and Fig. 2g and 2h show stratiform rainfall fraction in these regions. Ocean dynamics not considered in our simple model creates strong warm currents, which serve as local heat sources, locally deforming the T/M boundary. In this spillover region, convective rainfall fraction is higher than surroundings, extending tropical precipitation characteristics into the midlatitudes. This result evidences that the T/M theory has implications even for regional-scale phenomena.

As a caveat, though limited in extent, there exist some regions where the T/M ratio estimated by reanalysis appears tropical but the dynamics remain midlatitudinal. For example, at eastern ocean basin coasts such as offshore California, the estimated $\mathscr{T}/\mathscr{M}$ is high (Fig. 2b), yet midlatitude disturbances remain active in the geopotential height and potential vorticity fields (Fig. 2a and Supplementary Fig. 3c). One plausible cause of this discrepancy may be the neglect of zonal variations in the Rossby deformation radius L_R in the T/M ratio estimation by scaling, rather than a failure of the theory itself. For example, if the Rossby deformation radius L_R is larger than the zonal mean, as is the case in the stable eastern basin, the coarse-graining scale $L \sim \sqrt{10}L_{\mathrm{R}}$ chosen in our study leads to an overestimation of the T/M ratio.

Seasonal migration of the T/M boundary

The T/M boundary exhibits pronounced seasonal migration. Figure 3a shows the tropical region ($\mathscr{T}/\mathscr{M} > 10$) in January and July calculated from reanalysis data. The T/M boundary migrates northward in Northern Hemisphere summer, bringing Tokyo and Los Angeles into the tropics, and migrates southward in winter, bringing Sydney and São Paulo into the tropics. As shown in Fig. 3b, the zonal-mean Northern Hemisphere T/M boundary remains nearly constant around 20°N from December to April, then abruptly migrates northward from May, reaching its northernmost

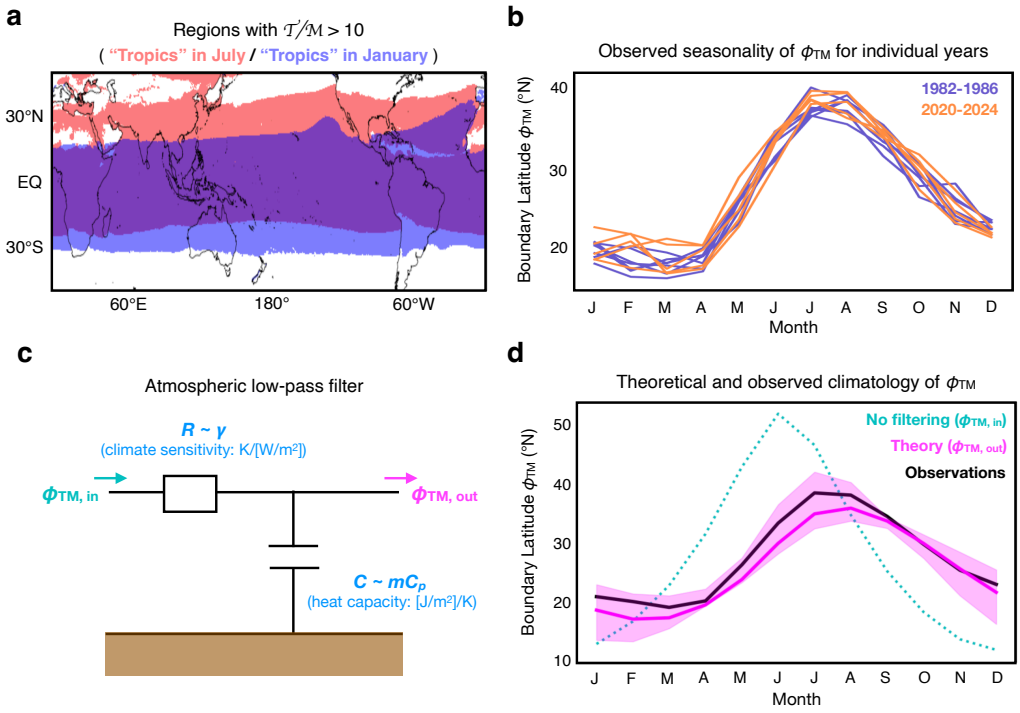

FIG. 3. **Seasonal migration of the T/M boundary.** (a) Regions with $\mathscr{T}/\mathscr{M} > 10$ during January (blue) and July (red). (b) Observed seasonality of zonal-mean ϕ_{TM} in the Northern Hemisphere during the first (purple, 1982-1986) and last (orange, 2020-2024) five years of the analysis period. (c) Schematic of the atmospheric low-pass filter explaining phase lag and amplitude damping in boundary migration. (d) Theoretical prediction (magenta) and observations (black) of the climatology of zonal-mean ϕ_{TM} in the Northern Hemisphere. In the former curve, the climate sensitivity of 3 °C/(2 × CO_2) is assumed. The magenta shaded area indicates the uncertainty of the theoretical prediction estimated by assuming that the climate sensitivity is 1.5-4.5 °C/(2 × CO_2). Also shown as blue dotted line is the ϕ_{TM} before the atmospheric low-pass filtering.

extent around 38°N in July before gradually migrating southward. Interestingly, maximum northward migration occurs not in June, when solar radiation is strongest, but one month later in July. Moreover, as shown later, the peak-to-peak amplitude of observed seasonal variation ($\sim 20°$) is substantially smaller than the amplitude predicted from solar radiation variation alone ($\sim 40°$).

To explain these features, theoretical prediction of seasonal variation proceeds as follows. First, we introduce seasonal radiation variation effects by replacing $\cos\phi$ in equation (4) with

$h_0 \sin\phi \sin\delta + \cos\phi \cos\delta \sin h_0$ (δ is solar declination, h_0 is hour angle). Next, to account for transient atmospheric response, we pass the calculated monthly latitudes through an "atmospheric low-pass filter" that incorporates climate sensitivity and atmospheric heat capacity (*see* Methods). Specifically, we use the RC low-pass filter circuit equation shown in Figure 3c:

$$\gamma m C_p \frac{d\phi_{\mathrm{TM,out}}(t)}{dt} + \phi_{\mathrm{TM,out}}(t) = \phi_{\mathrm{TM,in}}(t) \tag{6}$$

where t is time, γ is climate sensitivity, C_p is specific heat at constant pressure, and $\phi_{\mathrm{TM,in}}$ and $\phi_{\mathrm{TM,out}}$ are the T/M boundary latitudes before and after filtering, respectively.

This theoretical prediction (Figure 3d, magenta line) agrees well with observed seasonal variation (Figure 3d, black line). Here, observed ϕ_{TM} is obtained as the zonal-mean latitude of the $\mathscr{T}/\mathscr{M} = 10$ line based on reanalysis data. Following the Intergovernmental Panel on Climate Change (IPCC) Sixth Assessment Report[32], we assume climate sensitivity of 3°C per doubling of atmospheric CO_2 ($\gamma = 3$ °C/(2 × CO_2)). This filtering produces approximately one month phase lag and reduces amplitude to about 75%. Including climate sensitivity uncertainty of $\gamma = 1.5 - 4.5$ °C/(2 × CO_2), the theoretical curve agrees with observations within the uncertainty range. This agreement demonstrates that the transient response characteristics of the climate system play essential roles in the T/M boundary variations. It is also notable that the observed T/M boundary variations allow us to estimate the Earth's climate sensitivity as 1.5-4.5 °C/(2 × CO_2) in a simple, fundamental manner.

Seasonal variability of the T/M boundary latitude exhibits interannual variations and trends. Close inspection of Fig. 3b reveals that interannual variations and tropical expansion trends are particularly large in winter and summer, but are smaller during seasonal transitions in early summer and early autumn. The mechanisms generating such interannual variations and tropical expansion are explored further in subsequent sections.

Tropical expansion caused by global warming

Under global warming, mechanical source contribution decreases over most regions, and thermal source contribution becomes relatively more important. Figure 4a shows linear trends of $\log_{10}(\mathscr{T}/\mathscr{M})$ computed at each grid point over the past 40 years. Red regions show increasing T/M ratio (becoming more tropical), whereas blue regions show decreasing T/M ratio (becoming more midlatitudinal). Most regions appear red, particularly from the subtropics to the midlatitudes, indicating mechanical source contribution decreases and thermal source relative importance increases. We refer to this global tendency as the "global tropicalization".

The T/M boundary latitude has migrated poleward over the past 40 years, and this "tropical expansion" can be understood as a consequence of the aforementioned "global tropicalization." Figure 4b shows the time series of regional-mean $\log_{10}(\mathscr{T}/\mathscr{M})$ anomalies over the Northern Hemisphere subtropics (15°N-25°N) and the T/M boundary latitude. The high correlation of 0.76 between them demonstrates that the T/M boundary migration is a corollary of T/M ratio changes in the subtropical region.

To quantitatively understand the mechanism of global tropicalization, we decompose $\log_{10}(\mathscr{T}/\mathscr{M})$ trends into contributions from $\mathscr{T}$ and $\mathscr{M}$ changes, according to:

$$\Delta(\log_{10}(\mathscr{T}/\mathscr{M})) = \Delta(\log_{10}\mathscr{T}) - \Delta(\log_{10}\mathscr{M}) \tag{7}$$

where Δ denotes trends or anomalies. This decomposition, shown in Supplementary Fig. 4, indicates that the global tropicalization is primarily explained by the $\mathscr{M}$ change resulting from circulation weakening due to global warming[33]. The small $\mathscr{T}$ change is consistent with the Fixed Anvil Temperature mechanism, where adjustment processes in cumulonimbus suppress changes in radiative cooling rates under global warming[34].

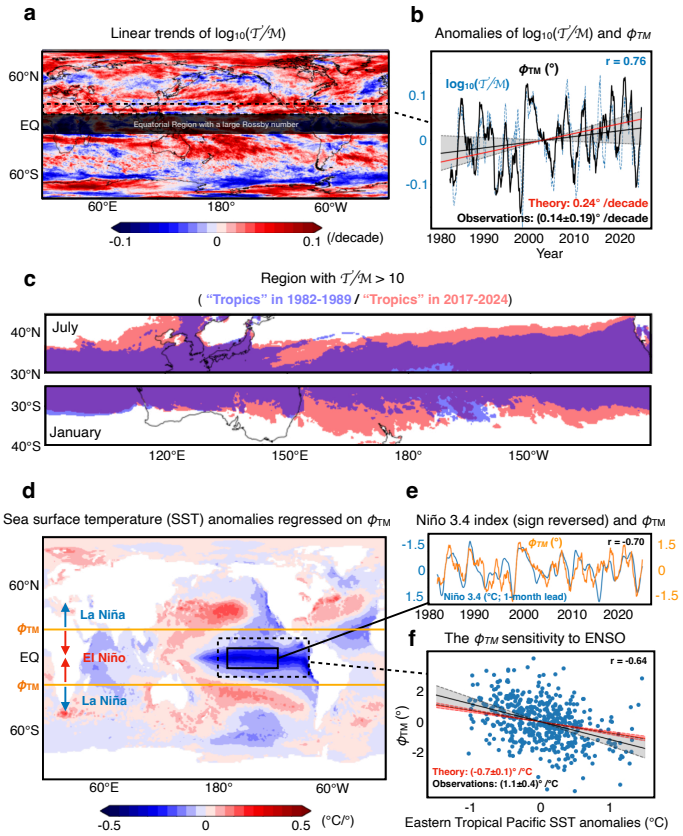

FIG. 4. **Trends and interannual variability of the T/M boundary.** (a) Linear trends of $\log_{10}(\mathscr{T}/\mathscr{M})$ at each grid point. The Northern Hemispheric subtropics (15°N-25°N) are shown as the black dashed box. (b) Observed monthly time series of regional-mean $\log_{10}(\mathscr{T}/\mathscr{M})$ over the Northern Hemispheric subtropics (blue dashed) and ϕ_{TM} (black solid). One-year running mean is applied. Red line shows the theoretically-predicted ϕ_{TM} trend, and black line shows the observed trend by the least-squares best fit. The uncertainty shown as the gray shaded area is estimated as the 95 % confidence interval. (c) Regions with temporal-mean $\mathscr{T}/\mathscr{M} > 10$ calculated for July (top) and January (bottom) of 1982-1989 (blue) and 2017-2024 (red). (d) Sea surface temperature (SST) anomalies regressed on detrended ϕ_{TM}. (e) Observed monthly SST anomalies averaged over the Niño 3.4 region (5°S-5°N, 170°W-120°W; black solid box in (d)) and monthly zonal-mean ϕ_{TM} anomalies. One-year running mean is applied. (f) Theoretical (red) and observed (black) sensitivity of zonal-mean ϕ_{TM} to the eastern tropical Pacific SST anomalies (black dashed box in (d)). The uncertainty of the theoretical prediction (red shaded area) is estimated by assuming that the climate sensitivity is 1.5-4.5 °C/(2 × CO_2). The uncertainty of the observed trend (black shaded area) is the 95 % confidence interval.

Our simple model of the T/M boundary, when incorporating circulation weakening as described by Held and Soden (2006)[33], predicts tropical expansion rates that agree with observed values within the uncertainty range. Specifically, global circulation weakens approximately 5%/°C, which is estimated as the difference between water vapor change (6.5%/°C) following the Clausius-Clapeyron relation and precipitation change (1.5%/°C) constrained by energy balance. The theoretical tropical expansion rate obtained by reducing typical wind speed U_0 by 5%/°C in equation (4) yields 0.24°/(decade) for the observed 0.8 °C warming over 40 years (*see* Methods). Figure 4b compares this theoretical trend with the observed trend, $0.14° \pm 0.19°$/(decade), which is statistically insignificant but consistent with numerous prior studies[22].

Although 0.24°/(decade) appears small, tropical expansion impacts are already apparent in some seasons and regions. Figure 4c compares the tropical region during the first and last 8 years of the analysis period for July (T/M boundary at maximum northward position) and January (maximum southward position). Tropical expansion is particularly pronounced in Asia-Oceania, where Beijing and New Zealand newly fell into the tropical territory over the 40-year period. Trend seasonality, evident in Fig. 3b and Supplementary Fig. 4d, further emphasizes tropical expansion impacts (Northern Hemisphere July: 0.37°/(decade)), allowing substantial updates to latitudinal limits. Thus, many regions previously unexposed to tropical climate will face sudden onset of tropical climate regimes in the near future.

Interannual variations explained by the El Niño-Southern Oscillation

The T/M boundary exhibits interannual variations in response to the El Niño-Southern Oscillation (ENSO), a prominent mode of climate variability on Earth. Figure 4d shows SST anomalies regressed onto the T/M boundary latitude anomalies, with clear ENSO-characteristic patterns visible in the tropical Pacific. Figure 4e shows time series of the Niño 3.4 index, which characterizes

the ENSO phase, and the T/M boundary latitude, revealing large negative correlation of -0.70. This negative correlation indicates that the T/M boundary migrates equatorward during El Niño episodes and poleward during opposite-phase La Niña.

Because global-mean temperature tends to increase during El Niño[35,36], one may find this ENSO response contradictory to global warming response. However, the T/M theory provides unified understanding of this difference based on heating spatial patterns and circulation response. Under global warming, circulation weakens due to constraints from water vapor transport accompanying global temperature rise, reducing mechanical sources and expanding tropics. Under El Niño, tropical eastern Pacific's local heating requires circulation intensification for heat redistribution, increasing mechanical sources and contracting tropics (Supplementary Fig. 5). This mechanism aligns with prior idealized atmospheric model studies, which showed that a broad heat source expands the tropics in a global warming-like manner, whereas a narrow heat source contracts tropics in an El Niño-like manner[11,20,37].

From this dynamical interpretation, the relationship between the eastern tropical Pacific SST increase and the circulation intensification can be estimated as follows:

$$\frac{dU_0}{dT} \sim \frac{R_d \rho_s L_v C_E U_{eq}}{8 C_v f U_0 m} \frac{dq_s}{dT} \approx 0.39 \text{ (m/s)/K} \tag{8}$$

(*see* Methods for details). Here, R_d is the gas constant for dry air, ρ_s is sea-level air density, L_v is latent heat, C_E is bulk exchange coefficient, U_{eq} is mean wind speed in the tropical eastern Pacific, and dq_s/dT is the temperature derivative of saturation specific humidity.

Transforming the ENSO circulation sensitivity into T/M boundary latitude sensitivity using equation (4), the theoretical value agrees with observations within the uncertainty range. Figure 4f compares this value with the observed sensitivity to tropical eastern Pacific SST. The T/M theory predicts that the Northern Hemisphere T/M boundary responds with sensitivity $-0.7^\circ \pm 0.1^\circ/^\circ\text{C}$

in the tropical eastern Pacific, whereas least-squares estimation of observed sensitivity yields $-1.1^\circ \pm 0.4^\circ/^\circ\mathrm{C}$.

Conclusions

The T/M theory provides a first-principles explanation of mechanisms that define the boundary between the tropics and the midlatitudes. The theory first establishes that the tropical region is where thermal source dominantly drives vertical motions, whereas the midlatitude region is where mechanical source also plays a significant role in determining vertical motions. The tropical-midlatitude boundary forms where mechanical sources become non-negligible, with a "phase transition" between climate zones occurring in this boundary region. Our simple model describes the essential mechanism of the T/M boundary latitude determination. This idealized model provides unified understanding across different timescale phenomena, i.e., seasonal variability, tropical expansion due to global warming, and the T/M boundary fluctuations forced by ENSO. Quantitative consistency between theoretical predictions and observations for these phenomena supports the validity of the T/M theory.

Singular phenomena emerge near the T/M boundary where thermal and mechanical source balance shifts delicately, forming a boundary layer region with unique characteristics. Within this layer, cooperative thermal and mechanical adjustments produce mesoscale phenomena that connect the two regions[38,39]. For example, as the boundary region characteristics, stationary fronts called "the Meiyu/Baiu front" emerge in June in East Asia; when crossing the boundary, tropical cyclones undergo extratropical transition. Furthermore, the presence of strong heat sources, such as the warm ocean currents near the T/M boundary, creates regions where the tropics intrude the midlatitudes. This "tropical spillover" plays roles in jet stream meridional migration[40,41], modulation of storm track zonal distribution[42], and oceanic decadal-scale variations[43]. In recent

years, the spatial resolution of observational data[44], general circulation models[45,46], and reanalysis data[47] is rapidly increasing. With these advances, atmospheric behaviors within the T/M boundary layer may be explainable as adjustment processes to balance the thermal and mechanical driving sources.

The T/M theory brings direct implications for climate change mitigation. Most extreme weather that threatens humanity, such as heavy rains, occurs via mesoscale phenomena. Therefore, understanding how large-scale constraints produce mesoscale phenomena is essential for disaster prevention. In addition, physical understanding of the "tropical expansion" contributes to improving future projection reliability for regional climate changes in the T/M boundary transit zones, where approximately half the global population resides[22]. This "tropical expansion" forces societal infrastructure reconstruction through discontinuous changes to agriculture and water resources[23]. The physical robustness of the T/M theory is expected to guide the mitigation and adaptation strategies for climate change[15,21,22], including the projected increase in wildfires and desertification associated with the poleward expansion of subtropical dry zones[23,48].

The T/M theory also has implications for other scientific disciplines. For instance, since terrestrial climate boundaries serve as vegetation boundaries, the T/M theory provides theoretical foundations for understanding shifts in habitable ranges for animals and plants[28,29]. Meanwhile, some migratory fishes move in opposite directions across the T/M boundary[49,50], suggesting the T/M theory may help elucidate marine ecosystems. Furthermore, the T/M theory is applicable to atmospheric circulation of other planets with different physical parameters (e.g., Mars)[24,25]. Comparison with other planets will offer a method to strengthen the plausibility of the theoretical meteorology, aiding deeper understanding of Earth's atmosphere.

References

[1] Ryu Shimabukuro, Tomohiko Tomita, and Ken-ichi Fukui. Update of global maps of Alisov's climate classification. Prog. Earth Planet. Sci., 10(1):1–18, 2023.

[2] Zhe Li and Qinghua Ding. A global poleward shift of atmospheric rivers. Sci. Adv., 10(41): eadq0604, 2024.

[3] Wolfgang Wicker, Emmanuele Russo, and Daniela IV Domeisen. A poleward storm track shift reduces mid-latitude heatwave frequency: insights from an idealized atmospheric model. Wea. Clim. Dyn., 6(3):965–979, 2025.

[4] Xiao Lu, Lin Zhang, Yuanhong Zhao, Daniel J Jacob, Yongyun Hu, Lu Hu, Meng Gao, Xiong Liu, Irina Petropavlovskikh, Audra McClure-Begley, et al. Surface and tropospheric ozone trends in the Southern Hemisphere since 1990: possible linkages to poleward expansion of the Hadley circulation. Sci. Bull., 64(6):400–409, 2019.

[5] Wenmin Zhang, Guy Schurgers, Josep Peñuelas, Rasmus Fensholt, Hui Yang, Jing Tang, Xiaowei Tong, Philippe Ciais, and Martin Brandt. Recent decrease of the impact of tropical temperature on the carbon cycle linked to increased precipitation. Nat. Comm., 14(1):965, 2023.

[6] Nathan L Stephenson. Climatic control of vegetation distribution: the role of the water balance. The American Naturalist, 135(5):649–670, 1990.

[7] I-Ching Chen, Jane K Hill, Ralf Ohlemüller, David B Roy, and Chris D Thomas. Rapid range shifts of species associated with high levels of climate warming. Science, 333(6045): 1024–1026, 2011.

[8] Isaac M Held and Arthur Y Hou. Nonlinear axially symmetric circulations in a nearly inviscid atmosphere. J. Atmos. Sci., 37(3):515–533, 1980.

[9] Christopher C Walker and Tapio Schneider. Eddy influences on hadley circulations: Simulations with an idealized gcm. J. Atmos. Sci., 63(12):3333–3350, 2006.

[10] Xavier J Levine and Tapio Schneider. Response of the hadley circulation to climate change in an aquaplanet gcm coupled to a simple representation of ocean heat transport. J. Atmos. Sci., 68(4):769–783, 2011.

[11] Xavier J Levine and Tapio Schneider. Baroclinic eddies and the extent of the Hadley circulation: An idealized GCM study. J. Atmos. Sci., 72(7):2744–2761, 2015.

[12] Casey C Hilgenbrink and Dennis L Hartmann. The response of Hadley circulation extent to an idealized representation of poleward ocean heat transport in an aquaplanet GCM. J. Climate, 31(23):9753–9770, 2018.

[13] Hu Yang, Gerrit Lohmann, Xiaoxu Shi, and Juliane Müller. Evaluating the mechanism of tropical expansion using idealized numerical experiments. Ocean-Land-Atmos. Res., 2:0004, 2023.

[14] Pengcheng Zhang, Nicholas J Lutsko, Spencer A Hill, and Shang-Ping Xie. Hadley cell dynamics in an axisymmetric single-layer model: Effects of parameterized eddies and equatorial heating. J. Atmos. Sci., 82(12):2757–2770, 2025.

[15] Dian J Seidel, Qiang Fu, William J Randel, and Thomas J Reichler. Widening of the tropical belt in a changing climate. Nature Geosci., 1(1):21–24, 2008.

[16] Osamu Miyawaki, Tiffany A Shaw, and Malte F Jansen. Quantifying energy balance regimes in the modern climate, their link to lapse rate regimes, and their response to warming. J. Climate, 35(3):1045–1061, 2022.

[17] Jian Lu, Gabriel A Vecchi, and Thomas Reichler. Expansion of the Hadley cell under global warming. Geophysical Research Letters, 34(6), 2007.

[18] Dargan MW Frierson, Jian Lu, and Gang Chen. Width of the hadley cell in simple and comprehensive general circulation models. Geophys. Res. Lett., 34(18), 2007.

[19] PF Freisen, JM Arblaster, C Jakob, and JM Rodríguez. Investigating tropical versus extratropical influences on the southern hemisphere tropical edge in the unified model. J. Geophys. Res. Atmos., 127(7):e2021JD036106, 2022.

[20] Polina Khapikova and Tapio Schneider. An energetic framework for understanding Hadley circulation width variations: Seasonal cycle, ENSO, and global warming. J. Atmos. Sci., 82 (11):2569–2580, 2025.

[21] Qiang Fu, Celeste M Johanson, John M Wallace, and Thomas Reichler. Enhanced mid-latitude tropospheric warming in satellite measurements. Science, 312(5777):1179–1179, 2006.

[22] Paul W Staten, Jian Lu, Kevin M Grise, Sean M Davis, and Thomas Birner. Re-examining tropical expansion. Nature Climate Change, 8(9):768–775, 2018.

[23] Natalie J Burls, Ross C Blamey, Benjamin A Cash, Erik T Swenson, Abdullah al Fahad, Mary-Jane M Bopape, David M Straus, and Chris JC Reason. The Cape Town “ day zero ” drought and Hadley cell expansion. Npj Clim. Atmos. Sci., 2(1):27, 2019.

[24] PL Read. Dynamics and circulation regimes of terrestrial planets. Planet. Space Sci., 59(10): 900–914, 2011.

[25] Adam P Showman, Robin D Wordsworth, Timothy M Merlis, and Yohai Kaspi. Atmospheric circulation of terrestrial exoplanets. Comp. Climatol. Terr. Planets, 1:277–326, 2013.

[26] Haoyu Tong, Tim Li, and Xiao Pan. Meridional shift of climatological tropical cyclone genesis location in the western North Pacific. Atmos. Sci. Lett., 25(11):e1263, 2024.

[27] Courtney Schumacher and Aaron Funk. Assessing convective-stratiform precipitation regimes in the tropics and extratropics with the GPM satellite radar. Geophys. Res. Lett., 50(14):e2023GL102786, 2023.

[28] Marten Scheffer, Steve Carpenter, Jonathan A Foley, Carl Folke, and Brian Walker. Catastrophic shifts in ecosystems. Nature, 413(6856):591–596, 2001.

[29] Gian-Reto Walther, Eric Post, Peter Convey, Annette Menzel, Camille Parmesan, Trevor JC Beebee, Jean-Marc Fromentin, Ove Hoegh-Guldberg, and Franz Bairlein. Ecological responses to recent climate change. Nature, 416(6879):389–395, 2002.

[30] Adam H Sobel, Johan Nilsson, and Lorenzo M Polvani. The weak temperature gradient approximation and balanced tropical moisture waves. J. Atmos. Sci., 58(23):3650–3665, 2001.

[31] Jule G Charney and NA Phillips. Numerical integration of the quasi-geostrophic equations for barotropic and simple baroclinic flows. J. Atmos. Sci., 10(2):71–99, 1953.

[32] Piers M. Forster, Trude Storelvmo, Kyle C. Armour, William Collins, Jean-Louis Dufresne, David Frame, Daniel J. Lunt, Thorsten Mauritsen, Matthew D. Palmer, Masahiro Watanabe, Martin Wild, and Huan Zhang. The Earth ' s energy budget, climate feedbacks, and

climate sensitivity. In Valérie Masson-Delmotte, Panmao Zhai, Anna Pirani, Sarah L. Connors, Clotilde Péan, Sophie Berger, Nada Caud, Yang Chen, Leah Goldfarb, Melinda I. Gomis, Mengtian Huang, Katherine Leitzell, Elisabeth Lonnoy, J. B. Robin Matthews, Thomas K. Maycock, Tim Waterfield, Ozge Yelekçi, Rong Yu, and Bohan Zhou, editors, Climate Change 2021: The Physical Science Basis, pages 923–1054. Cambridge University Press, Cambridge, United Kingdom and New York, NY, USA, 2021. doi: 10.1017/9781009157896.009.

[33] Isaac M Held and Brian J Soden. Robust responses of the hydrological cycle to global warming. J. Climate, 19(21):5686–5699, 2006.

[34] Dennis L Hartmann and Kristin Larson. An important constraint on tropical cloud-climate feedback. Geophys. Res. Lett., 29(20):12–1, 2002.

[35] Yu Kosaka and Shang-Ping Xie. Recent global-warming hiatus tied to equatorial Pacific surface cooling. Nature, 501(7467):403–407, 2013.

[36] Yu Kosaka and Shang-Ping Xie. The tropical Pacific as a key pacemaker of the variable rates of global warming. Nature Geosci., 9(9):669–673, 2016.

[37] Neil F Tandon, Edwin P Gerber, Adam H Sobel, and Lorenzo M Polvani. Understanding Hadley cell expansion versus contraction: Insights from simplified models and implications for recent observations. J. Climate, 26(12):4304–4321, 2013.

[38] Ryosuke Shibuya, Yukari Takayabu, and Hirotaka Kamahori. Dynamics of widespread extreme precipitation events and the associated large-scale environment using AMeDAS and JRA-55 data. J. Climate, 34(22):8955–8970, 2021.

[39] Yu-Xiang Qiao, Hirohiko Nakamura, and Tomohiko Tomita. Warming of the kuroshio current over the last four decades has intensified the meiyu-baiu rainband. Geophys. Res. Lett., 51(2):e2023GL107021, 2024.

[40] Tsubasa Kohyama, Yoko Yamagami, Hiroaki Miura, Shoichiro Kido, Hiroaki Tatebe, and Masahiro Watanabe. The Gulf stream and Kuroshio current are synchronized. Science, 374 (6565):341–346, 2021.

[41] Tsubasa Kohyama, Yoko Yamagami, Shoichiro Kido, Fumiaki Ogawa, and Hiroaki Miura. Interactive annular mode links jet stream-ocean coupling to decadal Northern Hemispheric warmth. 2025.

[42] Brian J Hoskins and Paul J Valdes. On the existence of storm-tracks. J. Atmos. Sci., 47(15): 1854–1864, 1990.

[43] Robert CJ Wills, David S Battisti, Cristian Proistosescu, LuAnne Thompson, Dennis L Hartmann, and Kyle C Armour. Ocean circulation signatures of north pacific decadal variability. Geophys. Res. Lett., 46(3):1690–1701, 2019.

[44] Boyin Huang, Chunying Liu, Viva Banzon, Eric Freeman, Garrett Graham, Bill Hankins, Tom Smith, and Huai-Min Zhang. Improvements of the daily optimum interpolation sea surface temperature (DOISST) version 2.1. Journal of Climate, 34(8):2923–2939, 2021.

[45] Hirofumi Tomita and Masaki Satoh. A new dynamical framework of nonhydrostatic global model using the icosahedral grid. Fluid Dynamics Research, 34(6):357, 2004.

[46] Ryusuke Masunaga, Tomoki Miyakawa, Takao Kawasaki, and Hisashi Yashiro. Flux adjustment on seasonal-scale sea surface temperature drift in NICOCO. J. Meteor. Soc. Japan, 101 (3):175–189, 2023.

[47] Hans Hersbach, Bill Bell, Paul Berrisford, Shoji Hirahara, András Horányi, Joaquín Muñoz-Sabater, Julien Nicolas, Carole Peubey, Raluca Radu, Dinand Schepers, et al. The era5 global reanalysis. Quarterly journal of the royal meteorological society, 146(730):1999–2049, 2020.

[48] Paul W Staten, Kevin M Grise, Sean M Davis, Kristopher B Karnauskas, Darryn W Waugh, Amanda C Maycock, Qiang Fu, Kerry Cook, Ori Adam, Isla R Simpson, et al. Tropical widening: From global variations to regional impacts. Bull. Amer. Meteor. Soc., 101(6): E897–E904, 2020.

[49] Minato Yasui and Noriyoshi Mori. The route of skipjack tuna (Katsuwonus Pelamis) in their migration into the coastal waters of Japan, as seen from, tagging results. Bull. Shizuoka Pref. Fish. Exp. Stn., 20:1–8, 1985.

[50] S Ito, M Ogura, T Tanabe, K Takeuchi, and M Nonaka. Estimation of the skipjack [katsuwonus pelamis] migration pattern by a skipjack general migration model. Bull. Tohoku Natl. Fish. Res. Inst., 60:41–48, 1998.

[51] James R Holton and Gregory J Hakim. An introduction to dynamic meteorology, volume 88. Academic press, 2013.

[52] Christopher S Bretherton, Martin Widmann, Valentin P Dymnikov, John M Wallace, and Ileana Bladé. The effective number of spatial degrees of freedom of a time-varying field. J. Climate, 12(7):1990–2009, 1999.

[53] Lixin Wu, Wenju Cai, Liping Zhang, Hisashi Nakamura, Axel Timmermann, Terry Joyce, Michael J McPhaden, Michael Alexander, Bo Qiu, Martin Visbeck, et al. Enhanced warming over the global subtropical western boundary currents. Nature Climate Change, 2(3):161–166, 2012.

[54] Guang Jun Zhang and Michael J McPhaden. The relationship between sea surface temperature and latent heat flux in the equatorial Pacific. J. Climate, 8(3):589–605, 1995.

[55] WG Large and S Pond. Open ocean momentum flux measurements in moderate to strong winds. J. Phys. Oceanogr., 11(3):324–336, 1981.

Methods

Scaling of $\mathscr{T}/\mathscr{M}$ applicable for the Earth's large-scale system

This section demonstrates that the scaling $\mathscr{T}/\mathscr{M} \sim J/(fU^2L_\mathrm{R}^2/L^2)$ shown on the right-hand side of equation (2) holds by requiring two properties characterizing Earth's large-scale phenomena: hydrostatic balance and quasi-geostrophic balance. Here, we assume the Northern Hemisphere with positive Coriolis parameter, though the same argument applies to the Southern Hemisphere by replacing f with $-f$. Below, we denote scales of physical variables by curly braces $\{\}$, and $\sim$ means "equal in scale."

From the definition introduced in equation (2):

$$\mathscr{T}/\mathscr{M} := \left| \frac{[\, j \,]}{[\, -C_\mathrm{p} DT/Dt \,]} \right| = \left| \frac{[\, j \,]}{-C_\mathrm{p} D[T]/Dt} \right| \tag{9}$$

Using the hypsometric equation based on hydrostatic balance:

$$Z_\mathrm{T} = \frac{R_\mathrm{d}[T]}{g} \ln \frac{p_1}{p_2} \tag{10}$$

we can eliminate $[T]$ from equation (9) to obtain:

$$\mathscr{T}/\mathscr{M} = \left| \frac{[\, j \,]}{[\, -g(C_\mathrm{p})/(R_\mathrm{d} \ln \frac{p_1}{p_2}) \cdot DZ_\mathrm{T}/Dt \,]} \right| \simeq \left| \frac{[\, j \,]}{-gDZ_\mathrm{T}/Dt} \right| \tag{11}$$

using $C_\mathrm{p}/(R_\mathrm{d} \ln \frac{p_1}{p_2}) = 7/(2\ln 10) \sim 1$. Here, p_1 and p_2 denote the surface pressure and the tropopause pressure, respectively, assuming the atmosphere consisting of a troposphere and a

stratosphere with distinct lapse rates. This assumption allows us to approximate the tropospheric vertical-mean temperature using Z_{T}, as described in the main text.

From the continuity equation, DZ_{T}/Dt can be expressed as:

$$\left\{\frac{DZ_{\mathrm{T}}}{Dt}\right\} \sim H\{\delta\} \tag{12}$$

where $\{\delta\}$ is divergence and H is typical tropospheric height. Furthermore, under quasi-geostrophic balance, which is valid when Rossby number $\mathrm{Ro} := U/fL$ is small (widely applicable to large-scale phenomena with $L \gtrsim 2000$ km, except near the equator; Supplementary Fig. 2), the divergence scale is $\{\delta\} \sim \mathrm{Ro}U/L$ (*see* Supplementary Text 2). Thus,

$$\left\{\frac{DZ_{\mathrm{T}}}{Dt}\right\} \sim H \cdot \mathrm{Ro}\frac{U}{L} \sim \frac{HU^2}{fL^2} \tag{13}$$

Using this with equation (11), the scale of $\mathscr{T}/\mathscr{M}$ becomes:

$$\{\mathscr{T}/\mathscr{M}\} \sim \frac{J}{fU^2 \cdot gH/f^2L^2} \sim \frac{J}{fU^2} \cdot \frac{L^2}{L_{\mathrm{R}}^2} \tag{14}$$

where we define $L_{\mathrm{R}} := \sqrt{gH}/f$. Since our main goal is to understand the importance of physical processes through scaling analysis rather than to compute precise local values, we hereafter use $\mathscr{T}$ and $\mathscr{M}$ without curly braces to denote their scales for simplicity.

Simplest theoretical model to predict the T/M boundary latitude

In the main text, we construct a static model shown in Fig. 1 to extract the essence of the T/M boundary. This simple model allows us to describe the first-principles mechanism to determine the T/M boundary latitude to the first order.

General idea

As described in the main text, we choose a horizontal scale satisfying $L \sim \sqrt{10}L_{\mathrm{R}}$ as a reasonable coarse-graining to resolve the T/M boundary, and reduce the T/M boundary condition $\mathscr{T}/\mathscr{M} \sim 10$

to the simple condition $J \sim fU^2$. Using this condition, we derive the T/M boundary latitude as follows.

First, we estimate the scale of diabatic heating $J(\phi)$ as a function of latitude ϕ, based on the difference between shortwave radiation (SW) received from the sun and longwave radiation (LW) lost to space. We assume that net radiative heating received by Earth (SW-LW) becomes an atmospheric heat source through either shortwave absorption by the atmosphere or sensible and latent heat fluxes from the surface. When net radiative heating is negative, it cools the atmosphere. In reality, approximately one-tenth of incident energy is transported by oceans, but as a zeroth-order approximation, we neglect ocean heat transport. Since solar zenith angle increases from equator to pole, SW decreases with the cosine of latitude. We assume that heat received by the atmosphere is homogenized through the large-scale atmospheric circulation on timescales much faster than the climate time scale, and thus, we use the global mean value for LW. In reality, LW also varies with latitude, but much more gradually than SW spatial variations.

Next, we estimate $f(\phi)U(\phi)^2$ as a function of latitude. Coriolis parameter $f(\phi)$ increases from equator to pole with the sine of latitude. Wind speed $U(\phi)$ also varies with latitude, but we specify $U_0 := U(\phi_{\mathrm{TM}})$ as the model input representing the typical wind speed at the T/M boundary. By this specification, we are also prescribing eddy viscosity in the model. In this study, for example, we have adopted U_0 = 10 m/s as the traditional scaling parameter for a representative tropospheric wind speed[51]. In any case, our model is not intended to precisely predict the climatological T/M boundary latitude, but rather to understand the essential mechanism behind its determination.

Finally, the equation $J(\phi) = f(\phi)U(\phi)^2$ yields two analytical solutions in $0 < \phi < \pi/2$. The solution closer to the equator, ϕ_{TM}, represents the T/M boundary latitude. The other solution ϕ_{MP}, whose existence is predicted a priori, represents the boundary between the midlatitude and polar (M/P) regions. The following subsections explain these procedures mathematically.

Derivation of $J(\phi)$ and $f(\phi)U(\phi)^2$

First, we derive the expression for $J(\phi)$. The SW energy flux received by the atmosphere at latitude ϕ, denoted $F^{\downarrow}(\phi)$, can be expressed using the equatorial value $F_0 := F^{\downarrow}(0)$ as $F^{\downarrow}(\phi) = F_0 \cos\phi$. Due to the radiative equilibrium, the global-mean LW, denoted $\overline{F^{\uparrow}}$, equals the global-mean SW:

$$\overline{F^{\uparrow}} = \frac{1}{4\pi R^2} \int_{-\pi/2}^{\pi/2} \int_0^{2\pi} (F_0^{\downarrow} \cos\phi) R^2 \cos\phi \, d\lambda \, d\phi \quad \Longrightarrow \quad \overline{F^{\uparrow}} = \frac{\pi}{4} F_0 \tag{15}$$

where R is the Earth's radius and λ is longitude. Therefore, diabatic heating per unit mass $J(\phi)$ is:

$$mJ(\phi) = |F^{\downarrow}(\phi) - \overline{F^{\uparrow}}| \quad \Longrightarrow \quad J(\phi) = \left| \frac{F_0}{m} \cos\phi - \frac{\pi}{4} \frac{F_0}{m} \right| \tag{16}$$

where m is the vertically-integrated atmospheric mass per unit area.

Then, $f(\phi)U(\phi)^2$ is expressed by substituting the Coriolis parameter definition:

$$f(\phi)U(\phi)^2 = 2\Omega \sin\phi (U(\phi))^2 \tag{17}$$

Analytical solution of $J(\phi) = f(\phi)U(\phi)^2$

Using the above expressions, the T/M boundary condition $J(\phi) = f(\phi)U(\phi)^2$ yields:

$$\left| \frac{F_0}{m} \cos\phi - \frac{\pi}{4} \frac{F_0}{m} \right| = 2\Omega \sin\phi (U(\phi))^2 \tag{18}$$

First, we consider the case where SW>LW, i.e., the argument of the absolute value is positive. Denoting this solution ϕ_{TM} and setting $U_0 := U(\phi_{\mathrm{TM}})$:

$$\frac{F_0}{m} \cos\phi_{\mathrm{TM}} - \frac{\pi}{4} \frac{F_0}{m} = 2\Omega \sin\phi_{\mathrm{TM}} U_0^2 \tag{19}$$

$$\Longleftrightarrow \qquad -2\Omega U_0^2 \sin\phi_{\mathrm{TM}} + \frac{F_0}{m} \cos\phi_{\mathrm{TM}} = \frac{\pi}{4} \frac{F_0}{m} \tag{20}$$

$$\Longleftrightarrow \qquad \sqrt{4\Omega^2 U_0^4 + \frac{F_0^2}{m^2}} \sin\left(\phi_{\mathrm{TM}} - \arctan\left(\frac{F_0}{2\Omega U_0^2 m} \right) \right) = \frac{\pi}{4} \frac{F_0}{m} \tag{21}$$

$$\Longleftrightarrow \qquad \phi_{\mathrm{TM}} = \arctan\left(\frac{F_0}{2\Omega U_0^2 m} \right) - \arcsin\left(\frac{\pi F_0}{4\sqrt{4\Omega^2 m^2 U_0^4 + F_0^2}} \right) \tag{22}$$

Under radiative equilibrium, the relation among longwave radiation $\overline{F^{\uparrow}} = \pi F_0/4$, solar constant S_0, and mean planetary albedo A is:

$$S_0(1-A)\cdot\pi R^2 = \overline{F^{\uparrow}}\cdot 4\pi R^2 \quad\Longrightarrow\quad F_0 = \frac{S_0(1-A)}{\pi} \tag{23}$$

The analytical solution for ϕ_{TM} is thus:

$$\phi_{\mathrm{TM}}(U_0) \;=\; \arctan\left(\frac{S_0(1-A)}{2\Omega U_0^2\pi m}\right) - \arcsin\left(\frac{S_0(1-A)}{4m\sqrt{4\Omega^2U_0^4 + S_0^2(1-A)^2/\pi^2m^2}}\right) \tag{24}$$

where $S_0 = 1{,}366\ \mathrm{W/m^2}$, $A = 0.3$, $m = 10{,}337\ \mathrm{kg/m^2}$. For example, if we adopt $U_0 = 10\ \mathrm{m/s}$ as a model input, the model yields $\phi_{\mathrm{TM}} \simeq 19.0^{\circ}$.

Next, we consider the case where SW<LW, i.e., the argument of the absolute value is negative. Denoting this solution ϕ_{MP}, we analytically obtain:

$$\phi_{MP}(U_0) \;=\; \pi - \arctan\left(\frac{S_0(1-A)}{2\Omega U_0^2\pi m}\right) - \arcsin\left(\frac{S_0(1-A)}{4m\sqrt{4\Omega^2U_0^4 + S_0^2(1-A)^2/\pi^2m^2}}\right) \tag{25}$$

This latitude ($\phi_{MP} \simeq 71.5^{\circ}$) is inappropriate as a T/M boundary solution, but represents the boundary between midlatitude and polar regions (M/P boundary) where radiative cooling and available potential energy conversion are equally important. However, in the Earth's polar regions, the M/P boundary appears less distinctly than the T/M boundary, likely due to large noise from lateral and lower boundary conditions.

Observational validation

Data

We have used the reanalysis data from the European Centre for Medium-Range Weather Forecasts Reanalysis version 5 (ERA5)[47], whose time span covers from 1982 through 2024. Spatial resolution is 0.25° in both longitude and latitude directions. The vertically-averaged diabatic heat-

ing rate per unit mass is calculated as:

$$[j] = \frac{Q_{\mathrm{rad}} + \mathrm{LH} + \mathrm{SH} - L_{\mathrm{v}} \nabla \cdot [\vec{F}_{\mathrm{v}}]}{m} \tag{26}$$

Here, radiative heating per unit area Q_{rad} is obtained by subtracting net radiation reaching the surface from net radiation reaching the top of atmosphere for both longwave and shortwave (ERA5 uses downward positive sign convention). LH and SH are obtained by applying negative signs to the downward latent and sensible heat flux data from the atmosphere to the surface provided per unit area. Since ERA5 provides vertically-integrated moisture divergence $\nabla \cdot [\vec{F}_{\mathrm{v}}]$ (hereafter [ ] denotes vertical integration), we multiplied by latent heat $L_{\mathrm{v}} = 2.5 \times 10^6$ J/kg to obtain horizontal latent heat transport $L_{\mathrm{v}} \nabla \cdot [\vec{F}_{\mathrm{v}}]$. The constant $m = [\rho]$ (ρ denotes density), the vertical integral of mass of atmosphere provided by ERA5, is used to convert per-unit-area to per-unit-mass quantities.

The J and fU^2 used for $\mathscr{T}/\mathscr{M}$ calculation are obtained as follows. For J, we take the absolute value of $[j]$ calculated from equation (26). For fU^2:

$$f = 2\Omega \sin \phi \tag{27}$$

$$U = [u] = \frac{1}{m} \sqrt{([\rho u])^2 + ([\rho v])^2} \tag{28}$$

using the Earth's angular velocity $\Omega = 7.2 \times 10^{-4}/\mathrm{s}$, with $[u]$ obtained by dividing the magnitude of vertically-integrated mass flux, which is also provided by ERA5, by m.

Observed sea surface temperature (SST) data in Fig. 4c, 4d, and 4e are obtained from the National Oceanic and Atmospheric Administration (NOAA) Optimal Interpolation SST (OISST) version 2 high-resolution dataset[44]. Spatial resolution was interpolated to 1° in both zonal and meridional directions for computational efficiency. The time span used in this study is from 1982 through 2024.

Statistical methods

Monthly climatology is calculated by averaging each variable for each calendar month. For analyses of monthly anomalies, the corresponding monthly climatology and linear trends are removed, except in the analysis of the global warming response, for which the linear trend is retained. The statistical significance of correlations and regressions is assessed using a two-tailed Student's t-test. To account for autocorrelation in the time series when estimating the effective degrees of freedom, we employ the formula proposed by Bretherton et al. (1999)[52]. The Niño 3.4 index is calculated as the regional-mean detrended SST anomalies over the Niño 3.4 region (5°N–5°S, 170°W–120°W).

"Virtual lighting" visualization of the geopotential height surface

Figure 2a shows shaded "relief" of the 500 hPa geopotential height surface with "virtual lighting" cast from a specific angle. This visualization technique, devised by the third author, produces spatial shading variations according to the gradient direction of the geopotential height surface at each point. Specifically, shading is configured to brighten if the dot product between the unit gradient vector and (2, -1) is large, such that slopes dipping from roughly southeast to northwest appear bright, whereas those dipping from northwest to southeast appear dark. This shading presents the "relief" of the geopotential height field three-dimensionally, offering a fine view of flow patterns that are difficult to visualize using standard contour plots.

Atmospheric low-pass filter

As shown in the main text, the maximum northward T/M boundary migration occurs not in June, when solar radiation is strongest, but approximately one month later in July. We attribute this response lag to the atmospheric heat capacity and the climate sensitivity (temperature rise per

W/m^2 radiative forcing), constructing the following "atmospheric low-pass filter":

$$\gamma m C_p \frac{d\phi_{\mathrm{TM,out}}(t)}{dt} + \phi_{\mathrm{TM,out}}(t) = \phi_{\mathrm{TM,in}}(t) \tag{29}$$

where $\phi_{\mathrm{TM,in}}(t)$ is the T/M boundary latitude anomaly before filtering, derivable theoretically by introducing seasonal radiation variations into the simple model (detailed later). $\phi_{\mathrm{TM,out}}(t)$ is the T/M boundary latitude anomaly after filtering, reproducing observed seasonal variations. The climate sensitivity γ has units K/(W/m^2) (inverse of the conventionally-used climate feedback parameter λ_c). C_{p} $(= 1{,}004\ \mathrm{J/(kg \cdot K)})$ is the specific heat at constant pressure for dry air, and m is vertically-integrated atmospheric mass per unit area as already used. The product $\gamma m C_p$ gives a time constant of this system with dimensions of time (units: s).

The atmospheric filter equation (29) can be derived as follows. For the region near the T/M boundary, the radiative budget equation gives:

$$m C_p \frac{d\Delta T(t)}{dt} = \Delta F^{\downarrow}_{\mathrm{TM}}(t) - \lambda_c \Delta T(t) \tag{30}$$

where $\Delta F^{\downarrow}_{\mathrm{TM}}(t)$ is the seasonal variation of shortwave radiation in this region, and $\lambda_c \Delta T(t)$ is the longwave feedback for a given temperature anomaly $\Delta T(t)$. Then, we assume that the T/M boundary latitude anomaly after filtering $\phi_{\mathrm{TM,out}}$ is proportional to the temperature anomaly $\Delta T(t)$, or $\phi_{\mathrm{TM,out}} = k\Delta T(t)$, where k is a constant. This proportionality is the first-order approximation of the warming response of the T/M boundary latitude as discussed in the main text. Similarly, $\phi_{\mathrm{TM,in}}(t) = k\Delta F^{\downarrow}_{\mathrm{TM}}(t)/\lambda_c$, meaning that $\phi_{\mathrm{TM,in}}(t)$ is the T/M boundary latitude anomaly corresponding to the radiative-equilibrium temperature, which is derived by not accounting for the transience of the Earth's atmosphere. Substituting $\Delta T(t) = \phi_{\mathrm{TM,out}}/k$ and $\Delta F^{\downarrow}_{\mathrm{TM}}(t) = \lambda_c \phi_{\mathrm{TM,in}}(t)/k$ into equation (30), we obtain equation (29), considering that $\gamma = 1/\lambda_c$.

The atmospheric low-pass filter can be understood through analogy with the RC low-pass filter circuit shown in Fig. 3c. For an RC low-pass filter circuit with input voltage $V_{\mathrm{in}}(t)$ and output

voltage $V_{\mathrm{out}}(t)$, Kirchhoff's second law gives:

$$RC\frac{dV_{\mathrm{out}}(t)}{dt} + V_{\mathrm{out}}(t) = V_{\mathrm{in}}(t) \tag{31}$$

Therefore, the climate sensitivity γ (the atmospheric heat capacity mC_p) corresponds to the resistance R (the capacitance C), so the time constant of the climate response γmC_p plays the same role as that of the filter RC, i.e., the e-folding time for a step function input.

The latitude $\phi_{\mathrm{TM,in}}(t)$ before filtering reaches its maximum in June and minimum in December, with meridional migration amplitude exceeding observations. Figure 3d's blue dashed line shows $\phi_{\mathrm{TM,in}}(t)$ obtained by modifying equation (18) to include seasonal radiation variations:

$$\frac{F_0}{m}(h_0 \sin\phi \sin\delta + \cos\phi \cos\delta \sin h_0) - \frac{\pi}{4}\frac{F_0}{m} = 2\Omega \sin\phi (U(\phi))^2 \tag{32}$$

where monthly-mean solar declination δ and hour angle h_0 at latitude ϕ are obtained from:

$$\delta := -23.44^\circ \cos\left(\frac{2\pi}{365}(N+10)\right) \tag{33}$$

$$h_0 := \arccos(-\tan\phi \tan\delta) \tag{34}$$

Here, N is the day of year. Since we focus on seasonal variations, we correct the bias from annual climatology. However, $\phi_{\mathrm{TM,in}}(t)$ obtained this way does not accurately reproduce observed ϕ_{TM} behavior (Fig. 3d, black line).

In contrast, the latitude $\phi_{\mathrm{TM,out}}(t)$ after passing through the filter reproduces observations well. The red line in Fig. 3d shows the theoretical prediction of $\phi_{\mathrm{TM,out}}(t)$ estimated using climate sensitivity according to IPCC AR6[32] as "3°C temperature increase for doubling CO_2 forcing (3.7 W/m^2)". This theoretical value is obtained as follows. First, we subtract the time-mean value $\overline{\phi_{\mathrm{TM,in}}}$ from the time series of $\phi_{\mathrm{TM,in}}(t)$, and perform the Fourier transform to obtain $\hat{\phi}_{TM,\mathrm{in}}(\omega)$. Then, we input $\hat{\phi}_{TM,\mathrm{in}}(\omega)$ into the Fourier-transformed version of equation (29):

$$\hat{\phi}_{TM,out}(\omega) = \frac{1}{1 + i\omega(\gamma mC_p)}\hat{\phi}_{TM,in}(\omega) \tag{35}$$

Finally, we take the inverse Fourier transform of the output $\hat{\phi}_{TM,out}(\omega)$, and add back the time-mean value $\overline{\phi_{\mathrm{TM,in}}}$. The shaded region in Fig. 3 indicates the theoretical prediction range for $\phi_{\mathrm{TM,out}}(t)$, which is estimated by assuming the uncertainty range of the climate sensitivity to be 1.5–4.5°C/(2×CO_2). This "atmospheric low-pass filter" delays the phase of seasonal variations by approximately one month, and attenuates the amplitude to about 65–85%. As a result, the theoretical prediction of T/M boundary latitude exhibits seasonal variations consistent with observations.

Theoretical considerations for the warming response of T/M ratio

Here we show the method for estimating the warming response of the T/M boundary using the simple model presented in the main text. Following Held and Soden (2006)[33], circulation changes under global warming are estimated as the difference between water vapor change rate (6.5%/K) following the Clausius-Clapeyron relation and precipitation change rate (1.5%/K) constrained by energy conservation, yielding approximately 5%/K global weakening. Substituting reduced typical wind speed $U_0 + \Delta U_0 = 9.5$ m/s ($\Delta U_0 < 0$) into equation (5):

$$\phi_{\mathrm{TM}}(U_0+\Delta U_0) = \arctan\left(\frac{S_0(1-A)}{2\Omega(U_0+\Delta U_0)^2\pi m}\right) - \arcsin\left(\frac{S_0(1-A)}{4m\sqrt{4\Omega^2(U_0+\Delta U_0)^4+S_0^2(1-A)^2/\pi^2m^2}}\right) \quad (36)$$

$$\simeq 20.2^\circ \quad (37)$$

Thus, the poleward shift of the T/M boundary per kelvin of global warming is:

$$\frac{d\phi_{\mathrm{TM}}(U_0)}{dT} \simeq \frac{\phi_{\mathrm{TM}}(U_0+\Delta U_0)-\phi_{\mathrm{TM}}(U_0)}{\Delta T} = \frac{20.2^\circ - 19.0^\circ}{1\ K} = 1.2^\circ/\mathrm{K} \quad (38)$$

Hence, the 0.8 K global warming over the past 40 years yields the tropical expansion rate of $1.2\ ^\circ/\mathrm{K} \times 0.8\ \mathrm{K}/(40\ \mathrm{yr}) = 0.24^\circ$/decade.

Note that the above discussion is based on global means, so this method cannot necessarily be used for explaining local trends. Indeed, tropical expansion has several exception regions. Over western boundary current regions, expansion occurs but circulation weakening does not solely

dominate. The recent strengthening of western boundary currents[53] means that T/M changes from increased diabatic heating from lower boundary contribute comparably to $\mathscr{M}$ changes. Additionally, only on the polar side of jet streams does the T/M ratio show opposite tendencies with weak "midlatitudinalization" rather than tropicalization. This opposite response is because the poleward jet shift enhances the circulation in this region, offsetting the increased diabatic heating effects (*see also* Supplementary Fig. 4).

Theoretical considerations for the sensitivity of $\mathscr{T}/\mathscr{M}$ to ENSO

Here we derive the T/M boundary sensitivity to ENSO presented in equation (8) of the main text. When El Niño occurs, the eastern equatorial Pacific SST rises with accompanying upward surface heat flux anomalies, which warms the entire tropical region due to the WTG characteristics. However, because this fast response of heating is confined in the tropical region, the slower atmospheric circulation then transports most of the heat poleward. Therefore, we assume that all of the heat associated with the El Niño event is used for circulation intensification (increasing $\mathscr{M}$), rather than for increasing $\mathscr{T}$ in the T/M boundary region. This assumption is consistent with Supplementary Fig. 5, which shows that the T/M response to ENSO is primarily explained as the $\mathscr{M}$ response.

Based on this assumption, the tropical heating per unit mass balances poleward heat transport:

$$J \sim C_{\mathrm{v}} U_0 \left\{ \frac{dT}{dy} \right\} \tag{39}$$

where C_{v} is the specific heat at constant volume for dry air. Meanwhile, due to the small Rossby number, thermal wind balance constrains meridional temperature gradient:

$$U_0 \sim \frac{R_{\mathrm{d}}}{f} \left\{ \frac{dT}{dy} \right\} \tag{40}$$

where R_d is the gas constant for dry air. Therefore, the tropical heating is estimated as:

$$J \sim \frac{C_\mathrm{v} f}{R_\mathrm{d}} U_0^2 \tag{41}$$

When ENSO-induced eastern tropical Pacific SST anomaly dT increases tropical heating by dJ and typical wind speed by dU_0, differentiating equation (41) with respect to T:

$$\frac{dJ}{dT} \sim \frac{2C_\mathrm{v} f U_0}{R_\mathrm{d}} \frac{dU_0}{dT} \tag{42}$$

Thus, ENSO-induced circulation (typical wind speed) change is:

$$\frac{dU_0}{dT} \sim \frac{R_\mathrm{d}}{2C_\mathrm{v} f U_0} \frac{dJ}{dT} \tag{43}$$

Next, we obtain this heating from local SST warming. When the tropical eastern Pacific SST increases 1 K as a regional-mean value, local atmospheric latent heat flux change dJ_local/dT can be estimated by bulk formula:

$$m \frac{dJ_\mathrm{local}}{dT} = \rho_\mathrm{s} L_\mathrm{v} C_\mathrm{E} U_\mathrm{eq} \frac{dq_\mathrm{s}}{dT} \simeq 38.0 \ (\mathrm{W/m^2})/\mathrm{K} \tag{44}$$

which agrees with observations to the first order[54]. Here, we use the surface air density $\rho_\mathrm{s} = 1.2$ kg/m^3, latent heat $L_v = 2.5 \times 10^6$ J/kg, bulk transfer coefficient for fair weather $C_E = 1.2 \times 10^{-3}$ from Large and Pond (1981)[55], mean wind speed in the tropical eastern Pacific $U_\mathrm{eq} = 8$ m/s. From the Clausius-Clapeyron relation:

$$\frac{1}{q_\mathrm{s}} \frac{dq_\mathrm{s}}{dT} = 0.060/\mathrm{K} \quad \Longrightarrow \quad \frac{dq_\mathrm{s}}{dT} = 1.32 \times 10^{-3}/\mathrm{K} \tag{45}$$

using 27°C value (December climatology in the tropical eastern Pacific). Since the tropical eastern Pacific (180°W–90°W, 15°S–15°N) occupies approximately one-quarter of the tropical area, this local latent heating is distributed over four times the area when considering the total tropical heating dJ/dT. Therefore, we obtain:

$$\frac{dJ}{dT} \sim \frac{1}{4} \frac{dJ_\mathrm{local}}{dT} = \frac{\rho_\mathrm{s} L_\mathrm{v} C_\mathrm{E} U_\mathrm{eq}}{4m} \frac{dq_\mathrm{s}}{dT} \tag{46}$$

Finally, substituting equation (46) into equation (43), circulation intensification per 1 K tropical eastern Pacific warming is:

$$\frac{dU_0}{dT} \sim \frac{R_{\mathrm{d}}\rho_{\mathrm{s}}L_{\mathrm{v}}C_{\mathrm{E}}U_{\mathrm{eq}}}{8C_{\mathrm{v}}fU_0m}\frac{dq_{\mathrm{s}}}{dT} \simeq 0.39\ (\mathrm{m/s})/\mathrm{K} \tag{47}$$

using $m = 1.03 \times 10^4$ kg/m^2, $R_{\mathrm{d}} = 287$ J/(kg$\cdot$K), $C_{\mathrm{v}} = 717$ J/(kg$\cdot$K), $f = 2\Omega\sin(19.0^\circ) = 4.7 \times 10^{-5}/s$.

We use the T/M theory's analytical solution $\phi_{\mathrm{TM}}(U_0)$ to convert circulation intensification to boundary latitude change. Based on equation (47), when 1 K SST change produces typical wind speed $U_0 + \Delta U_0 = 10.39$ m/s, equation (24) gives $\phi_{\mathrm{TM}}(U_0 + \Delta U_0) = 18.1^\circ$. Thus, ENSO-induced T/M boundary latitude variation is:

$$\frac{d\phi_{\mathrm{TM}}(U_0)}{dT} \simeq \frac{\phi_{\mathrm{TM}}(U_0+\Delta U_0) - \phi_{\mathrm{TM}}(U_0)}{\Delta T} = \frac{18.1^\circ - 19.0^\circ}{1\ K} = -0.9^\circ/\mathrm{K} \tag{48}$$

Accounting for atmospheric low-pass filter effects obtained in the seasonal variability analysis (phase lag is one month, and amplitude reduces to 65-85% for climate sensitivity 1.5-4.5 K/(2 $\times$ CO_2)):

$$\left(\frac{d\phi_{\mathrm{TM}}(U_0)}{dT}\right)_{\mathrm{low-pass}} = (-0.7^\circ \pm 0.1^\circ)/\mathrm{K} \tag{49}$$

which predicts that the T/M boundary latitude shifts equatorward by 0.7° per 1 K tropical eastern Pacific warming.

Data availability

The ERA5 reanalysis data used in this study is available at `https://cds.climate.copernicus.eu/datasets/reanalysis-era5-pressure-levels-monthly-means?tab=download`. The NOAA OISST high resolution data set used in Fig. 4 is available at `https://www.esrl.noaa.gov/psd/data/gridded/data.noaa.oisst.v2.highres.html`.

Code availability

This study is theoretical in nature and does not involve large-scale numerical simulations. Simple scripts are used for illustrative calculations and figure generation. No specialized code is required to reproduce the main results, which can be obtained directly from the equations presented in the paper.

Acknowledgments

During the preparation of this article, the authors have used Claude 3 and ChatGPT 5.2 for AI-assisted copy editing. After using this service, the authors reviewed and edited the content as needed, and the authors take full responsibility for the content of the publication. The first author is supported by Japan Society for the Promotion of Science (JSPS) KAKENHI Grant Numbers JP23H01241 and JP23K13169, and by the Ministry of Education, Culture, Sports, Science and Technology (MEXT) program for the advanced studies of climate change projection (SENTAN) Grant Number JPMXD0722680395. The second author is supported by JSPS Kakenhi Grant Number JP23K25939. This project is also supported by the Sumitomo Foundation as one of their Environmental Research Projects, and by the Joint Research Program of the Institute of Low Temperature Science, Hokkaido University (25S002). We thank John M. Wallace for providing useful comments.

Author contributions

T.K. led the project, performed all analyses, and wrote the manuscript. H.M. conceived the idea to solve the tropical-midlatitude connection as a boundary layer problem. K.Y. developed the visualization of the virtual lighting in Fig. 2 and improved the mathematical formulation. All authors reviewed and edited the manuscript.

Competing intests

The authors declare no competing interests.

Additional information

Supplementary Information is available for this paper.

Correspondence and requests for materials should be addressed to Tsubasa Kohyama (tsubasa@is.ocha.ac.jp).

Peer review information (This part will be completed by Nature staff during proofing.)

Reprints and permissions information is available at www.nature.com/reprints.

Supplementary information for

"First-principles theory for Earth's tropical-midlatitude climate boundary"

Tsubasa Kohyama*, Hiroaki Miura, and Kazuya Yamazaki

Department of Information Sciences, Ochanomizu University, Tokyo, Japan

Department of Earth and Planetary Science, The University of Tokyo, Tokyo, Japan

Information Technology Center, The University of Tokyo, Tokyo, Japan

Correspondence and requests for materials should be addressed to Tsubasa Kohyama (tsubasa@is.ocha.ac.jp)

Contents

Supplementary Text 1. Enthalpy revisited

Definition

The T/M theory is grounded in thermodynamics expressed through specific enthalpy per unit mass of an ideal gas air parcel:

$$h := c_{\mathrm{v}} T + p\alpha \tag{1}$$

where c_{v} is specific heat at constant volume, T is temperature, p is pressure, and α is specific volume. The first term on the right-hand side, $c_{\mathrm{v}}T$, is the internal energy per unit mass of the air parcel. The second term, $p\alpha$, is the "pressure-volume energy" possessed by the "mechanical process", i.e., the dynamical mechanism external to the air parcel that maintains the space occupied by the air parcel. This "pressure-volume energy" is the energy required to maintain a volume α for a gas with pressure p, and it is stored in the mechanical process, not in the air parcel.

To clarify the physical entity of enthalpy, consider the simple system shown in Supplementary Fig. 1a. In this system, a container with gas (mass m, pressure p, temperature T, volume $V = Sh$) is enclosed by a smooth piston of mass M at height h above the bottom in a perfect vacuum with a gravitational field g. We assume that the weight of the piston Mg and the pressure force exerted by the gas on the piston pS are always in balance, maintaining an equilibrium state. In other words, the piston can move quasi-statically while maintaining constant pressure inside. In this system, the total energy of the system including both the gas and the piston (the sum of the internal energy of the gas $mc_{\mathrm{v}}T$ and the gravitational potential energy of the piston $Mgh = pV$) is equal to the enthalpy $mh = mc_{\mathrm{v}}T + pV$.

Most importantly, while the internal energy $mc_{\mathrm{v}}T$ is stored in the gas, the "pressure-volume energy" pV is stored as the potential energy of the piston in the mechanical process, not in the gas. For example, suppose the gas were instantaneously liquefied and removed from the system

over an infinitesimally short time. In this case, while the internal energy of the system immediately becomes zero, the potential energy pV required to maintain the void space in the container remains stored in the mechanical process (the piston) during the brief moment before the piston begins to fall to the bottom of the container.

Enthalpy representation of the first law of thermodynamics

The first law of thermodynamics expressed using enthalpy is:

$$dh = \delta q + \alpha dp \tag{2}$$

(where δq is the diabatic heating). Here, using the equation of state for an ideal gas and Mayer's relation:

$$dh = c_{\mathrm{v}} dT + d(p\alpha) = c_{\mathrm{v}} dT + RdT = (c_{\mathrm{v}} + R)dT = c_{\mathrm{p}} dT \tag{3}$$

(where R is the gas constant and c_{p} is specific heat at constant pressure), we obtain:

$$\boxed{-\alpha dp = \delta q - c_{\mathrm{p}} dT} \tag{4}$$

which is the theoretical foundation of this study.

The first law of thermodynamics mandates that any expansion or compression of an air parcel can be expressed as a combination of two distinct processes: an isothermal process that permits heat exchange with its environment, and an adiabatic process that is driven purely by mechanics. These two processes can be illustrated using the piston example (Supplementary Fig. 1b). If the piston is lightened by an amount $-dM$, the gas will expand and depressurize. The first law of thermodynamics requires that the physical process realizing this gas expansion can be decomposed into a combination of two different types of processes. One process is isothermal expansion: the gas is allowed to expand while covered by a heat bath (maintaining $dT = 0$), allowing heat inflow

($\delta q > 0$). The other process is adiabatic expansion: the gas is allowed to expand while covered by a thermal insulator (maintaining $\delta q = 0$), allowing temperature to decrease ($dT < 0$).

Equation (4) reveals that, to realize air parcel expansion (depressurization), two distinct enthalpy sources exist that are clearly scale-separated: the "thermal source" (δq), a molecular-scale process, and the "mechanical source" ($-c_{\mathrm{p}} dT$), a macro-scale process at which temperature is definable as a statistical property of the molecular ensemble. Expansion of an air parcel is isothermal-like if the thermal source is dominant, and adiabatic-like if the mechanical source is dominant.

Based on local thermodynamic conditions within the air parcel, the thermal source j realizes isothermal expansion (compression) through heating (cooling) from molecular-scale processes. For purely thermal isothermal expansion or compression to occur, temperature adjustment with the surroundings must be sufficiently fast compared to the pressure adjustment timescale. Examples in the climate system include heating from solar radiation, sensible and latent heating, and radiative cooling. In these cases, the air parcel achieves temperature adjustment with the surroundings through gravity wave dissipation. Particularly in the tropics, gravity waves are not interfered with by Earth's rotation effects, so temperature adjustment with surroundings is carried out efficiently.

Based on large-scale dynamic conditions outside the air parcel, the mechanical source $-c_{\mathrm{p}} dT$ realizes adiabatic expansion (compression) through changes in a statistical property defined at the molecular ensemble scale. For purely mechanical adiabatic expansion or compression to occur, temperature adjustment with the surroundings must be sufficiently slow compared to the pressure adjustment timescale. Examples in the climate system include external pressure changes induced by cold and warm air advection in the surroundings. Here, again, the air parcel achieves temperature adjustment with the surroundings through gravity wave dissipation. Particularly in the midlatitudes, gravity waves possess dispersive properties due to Earth's rotation effects, so they

cannot efficiently transport energy beyond the Rossby deformation radius, and temperature adjustment with the surroundings tends to be slow.

In atmospheric dynamics, assuming that such adjustment occurs quasi-statically while maintaining local thermodynamic equilibrium, the first law of thermodynamics is employed as a time-evolution equation in the form:

$$\boxed{-\alpha\omega = j - c_{\mathrm{p}}\frac{DT}{Dt}} \tag{5}$$

Here, $\omega := Dp/Dt$ is the pressure tendency, j is the diabatic heating rate, and DT/Dt is the temperature tendency. The two terms on the right-hand side of this equation represent the thermal source and mechanical source realizing pressure changes, which are equivalent to vertical motion under hydrostatic balance. Strictly speaking, since these are quantities per unit time, they should be called "the increasing rate" of the thermal and mechanical sources, but in this study, we refer to them simply as thermal source and mechanical source as long as it does not cause confusion.

Importantly, the "contribution ratio" of thermal and mechanical sources that realizes pressure changes (i.e., vertical motions) is not determined by the properties of the air parcel itself, but rather by the intrinsic properties of the mechanical process. For example, in the aforementioned piston analogy, if the piston is surrounded by a heat bath, the thermal source realizes the pressure change, whereas if it is surrounded by thermal insulation, the mechanical source realizes the pressure change; the state of the gas itself is irrelevant. Conversely, by manipulating the effective thermal conductivity of the heat bath or insulation, one can choose which enthalpy source supplies the pressure change.

Since the mechanical process in the atmosphere varies regionally, regional variations also emerge in which enthalpy source (thermal or mechanical) more readily supplies the energy needed for pressure changes. Specifically, the rate of heat exchange and temperature adjustment with the surroundings is largely constrained by the geographical distributions of fundamental parameters,

such as radiation and rotation. Then, the regional characteristics of the "contribution ratio" of thermal and mechanical sources in realizing pressure changes generates geographic diversity in atmospheric circulation structure and response characteristics.

In particular, under hydrostatic and quasi-geostrophic balance, the thermal source tends primarily to drive the atmosphere in the vertical direction with adjustment occurring through horizontal motion, whereas the mechanical source tends primarily to drive the atmosphere in the horizontal direction with adjustment occurring through vertical motion. Indeed, in the thermally-driven case, buoyancy imposes very localized vertical acceleration, and the magnitude of horizontal divergence is adjusted to satisfy the continuity equation (Sobel et al. 2001). Conversely, in the mechanically-driven case, large-scale potential vorticity conservation drives horizontal flow, and vertical motion is adjusted to satisfy the continuity equation (Supplementary Text 2).

The T/M ratio

In the main text, based on the first law of thermodynamics shown in equation (5), we define the Thermal-Mechanical ratio. This dimensionless number represents the relative importance of thermal and mechanical sources for driving vertical motion:

$$\mathscr{T}/\mathscr{M} := \left| \frac{[\, j \,]}{[\, -c_{\mathrm{p}} DT/Dt \,]} \right| \simeq \left| \frac{[\, j \,]}{gDZ_{\mathrm{T}}/Dt} \right| \sim \frac{J}{fU^2} \cdot \frac{L^2}{L_{\mathrm{R}}^2} \tag{6}$$

(*see also* Methods). $\mathscr{T}/\mathscr{M}$ is defined at each location and time.

$\mathscr{T}/\mathscr{M}$ is different from the reciprocal of the efficiency of a local heat engine, $1/\mathscr{E}$, where $\mathscr{E} := p(D\alpha/Dt)/j_H$. First of all, $\mathscr{T}$ is defined as the "net" heat source $j = j_H - j_L$ (the difference between the heating source j_H and cooling source j_L), not solely the heating source j_H as would appear in the denominator of $\mathscr{E}$. In addition, $\mathscr{M}$ is defined using the mechanical source $-c_{\mathrm{p}} DT/Dt$, not the work done by the gas $pD\alpha/Dt$ as would appear in the numerator of $\mathscr{E}$.

Note on the relationship with dry static energy

In atmospheric dynamics, dry static energy is sometimes used, defined as enthalpy plus the gravitational potential energy of the air parcel:

$$s := h + gZ = c_{\mathrm{v}}T + p\alpha + gZ = c_{\mathrm{v}}T + RT + gZ = c_{\mathrm{p}}T + gZ \tag{7}$$

where g is gravitational acceleration and Z is geopotential height. This gZ is the gravitational potential energy of the air parcel itself, not the pressure-volume energy $p\alpha$ stored in the mechanical process to maintain the air parcel's space. In the piston example of Supplementary Fig. 1a, this gZ corresponds to the potential energy of the gas when the container is at height Z above the ground.

Under the hydrostatic balance approximation, $\alpha\omega \simeq -gDZ/Dt$ holds, so the first law of thermodynamics can be rewritten using dry static energy as:

$$\frac{Ds}{Dt} \simeq j \tag{8}$$

However, the dry static energy representation obscures the role of the mechanical source as an atmospheric driver, so it is not used in this study.

Supplementary Text 2. Dynamical "phase transition" across the $\mathscr{T}/\mathscr{M}$ boundary

In this Supplementary Text, to understand the details of the dynamical phase transition that occurs at the T/M boundary, we discuss flows with small Rossby number in a shallow-water system on a β-plane. The scaling $\mathscr{T}/\mathscr{M} \sim J/(fU^2L_{\mathrm{R}}^2/L^2)$ used in the main text is obtained when assuming small Rossby number flow for dynamical variables that are vertically averaged under the hydrostatic balance assumption. Therefore, it is in complete correspondence with the assumptions of the equation system used below. Using this correspondence, we show that the WTG system is derived when $\mathscr{T}/\mathscr{M} \to \infty$, and the QGPV conservation system is derived when $\mathscr{T}/\mathscr{M} \to 0$. In both of these systems, gravity waves are filtered out to extract the essence of large-scale dynamics.

Basic equation

The basic equations considered here are as follows:

$$\begin{cases} \dfrac{\partial u}{\partial t} + \vec{u}\cdot\vec{\nabla}u - fv = -g\dfrac{\partial \eta}{\partial x} & \text{(9a)} \\ \dfrac{\partial v}{\partial t} + \vec{u}\cdot\vec{\nabla}v + fu = -g\dfrac{\partial \eta}{\partial y} & \text{(9b)} \\ \dfrac{\partial \eta}{\partial t} + \vec{u}\cdot\vec{\nabla}\eta + (H+\eta)(\vec{\nabla}\cdot\vec{u}) = \dfrac{j}{g} & \text{(9c)} \end{cases}$$

where u is the zonal wind, v is the meridional wind, $\vec{u} := (u, v)$ is the horizontal wind vector, g is gravitational acceleration, η is height perturbation, H is equivalent depth, j is the net heat source, and the Coriolis parameter is $f = f_0 + \beta y$.

Using Rossby number $\mathrm{Ro} := U/f_0L$ and Burger number $\mathrm{Bu} := (L_{\mathrm{R}}/L)^2 = gH/f_0^2L^2$, and typical heating scale $J \sim \mathrm{Ro}\,\mathscr{J}$, we nondimensionalize the variables by defining the scale of each variable

as follows[1]:

$$(u,v) = U(\hat{u},\hat{v}) \tag{10}$$

$$(x,y) = L(\hat{x},\hat{y}) \tag{11}$$

$$\eta = \mathrm{BuRo}H\hat{\eta} = \frac{f_0 UL}{g}\hat{\eta} \tag{12}$$

$$\beta = \mathrm{Ro}\frac{f_0}{L}\hat{\beta} \tag{13}$$

$$j = J\hat{j} = \mathrm{Ro}\,\mathscr{J}\,\hat{j} \tag{14}$$

These scalings are chosen so that geostrophic balance holds when the Rossby number is sufficiently small (Ro $\ll 1$), with $f_0 U \sim g\{\eta\}/L$ and the effects of β and j being negligible.

The scaling of time t is not straightforward, because the timescales of the momentum equations and the continuity equation are not necessarily equal. First, the timescale in the momentum equations is determined by the advective timescale L/U, so we nondimensionalize it as:

$$t = \frac{L}{U}\hat{t} \tag{15}$$

Then, the timescale in the continuity equation is determined roughly by the response timescale of the height field (pressure field) to divergence and convergence. Although this timescale has not yet been determined, for convenience of exposition, we use the divergence scale RoU/L derived later and write:

$$\left\{\frac{D\eta}{Dt}\right\} \sim \left\{H\left(\frac{\partial u}{\partial x}+\frac{\partial v}{\partial y}\right)\right\} \quad\Longrightarrow\quad \frac{\{\eta\}}{T} \sim H\mathrm{Ro}\frac{U}{L} \tag{16}$$

This scaling is justified by the fact that the resulting equations do not become inconsistent. Substituting equation (12) into this relation determines the timescale of the continuity equation as

[1]The Burger number used here has a reciprocal relationship with the definition given by Sobel et al. (2001), Bu $:= (L/L_\mathrm{R})^2$, but here we follow the convention in fluid dynamics.

$T \sim (L/U)/\mathrm{Bu}$. That is, the time t in the continuity equation is nondimensionalized as:

$$t = \frac{L}{U\mathrm{Bu}}\hat{t} \tag{17}$$

Using these scalings, the nondimensional equations are:

$$\begin{cases} \mathrm{Ro}\left(\dfrac{\partial \hat{u}}{\partial \hat{t}} + \hat{\vec{u}}\cdot\hat{\vec{\nabla}}\hat{u}\right) - (1+\mathrm{Ro}\hat{\beta}\hat{y})\hat{v} = -\dfrac{\partial \hat{\eta}}{\partial \hat{x}} & \text{(18a)} \\ \mathrm{Ro}\left(\dfrac{\partial \hat{v}}{\partial \hat{t}} + \hat{\vec{u}}\cdot\hat{\vec{\nabla}}\hat{v}\right) + (1+\mathrm{Ro}\hat{\beta}\hat{y})\hat{u} = -\dfrac{\partial \hat{\eta}}{\partial \hat{y}} & \text{(18b)} \\ \mathrm{Ro}\left(\dfrac{\partial \hat{\eta}}{\partial \hat{t}} + \hat{\vec{u}}\cdot\hat{\vec{\nabla}}\hat{\eta} + \dfrac{\hat{\eta}}{\mathrm{Bu}}\hat{\vec{\nabla}}\cdot\hat{\vec{u}}\right) + \hat{\vec{\nabla}}\cdot\hat{\vec{u}} = \mathrm{Da}\hat{j} & \text{(18c)} \end{cases}$$

Here, the Damköhler number is defined as:

$$\mathrm{Da} := \frac{JL}{gHU} = \mathrm{Ro}\frac{\mathscr{J}L}{gHU} \tag{19}$$

The Damköhler number is a nondimensional number conventionally used in chemical engineering to represent the ratio of the reaction rate to the transport rate. Here, it represents the ratio of the heating response (J/gH) to the advection (U/L). [2]

Rossby number expansion

Considering large-scale dynamics with $\mathrm{Ro} \ll 1$, we perform a Rossby number expansion of the basic equations:

$$\begin{cases} \hat{u} = \hat{u_0} + \mathrm{Ro}\hat{u_1} + \mathrm{Ro}^2\hat{u_2} + \cdots & \text{(20a)} \\ \hat{v} = \hat{v_0} + \mathrm{Ro}\hat{v_1} + \mathrm{Ro}^2\hat{v_2} + \cdots & \text{(20b)} \\ \hat{\eta} = \hat{\eta_0} + \mathrm{Ro}\hat{\eta_1} + \mathrm{Ro}^2\hat{\eta_2} + \cdots & \text{(20c)} \\ \hat{j} = \hat{j_0} + \mathrm{Ro}\hat{j_1} + \mathrm{Ro}^2\hat{j_2} + \cdots & \text{(20d)} \end{cases}$$

[2] In other words, it is the ratio of "advective transport time (L/U)" to "adjustment time of the field to divergence/convergence by heating ($gH/\{j\}$)". For example, the larger the heating, the more energy is injected into the system per unit time, the shorter the time required to change the dynamical field, and the smaller the role of advection.

Substituting these into equations (18a)-(18c), the equations of $O(1)$ are:

$$\begin{cases} -\hat{v_0} = -\dfrac{\partial \hat{\eta}_0}{\partial \hat{x}} & \text{(21a)} \\ \hat{u_0} = -\dfrac{\partial \hat{\eta}_0}{\partial \hat{y}} & \text{(21b)} \\ \hat{\vec{\nabla}} \cdot \vec{u_0} = 0 & \text{(21c)} \end{cases}$$

and those of $O(\mathrm{Ro})$ are:

$$\begin{cases} \dfrac{\partial \hat{u_0}}{\partial \hat{t}} + \hat{\vec{u_0}} \cdot \hat{\vec{\nabla}} \hat{u_0} - \hat{v_1} - \hat{\beta} \hat{y} \hat{v_0} = -\dfrac{\partial \hat{\eta}_1}{\partial \hat{x}} & \text{(22a)} \\ \dfrac{\partial \hat{v_0}}{\partial \hat{t}} + \hat{\vec{u_0}} \cdot \hat{\vec{\nabla}} \hat{v_0} + \hat{u_1} + \hat{\beta} \hat{y} \hat{v_0} = -\dfrac{\partial \hat{\eta}_1}{\partial \hat{y}} & \text{(22b)} \\ \dfrac{\partial \hat{\eta}_0}{\partial \hat{t}} + \hat{\vec{u_0}} \cdot \hat{\vec{\nabla}} \hat{\eta}_0 + \dfrac{\hat{\eta}_0}{\mathrm{Bu}} \hat{\vec{\nabla}} \cdot \hat{\vec{u_0}} + \hat{\vec{\nabla}} \cdot \hat{\vec{u_1}} = \dfrac{JL}{gHU} \hat{j}_0 & \text{(22c)} \end{cases}$$

Rewriting these equations in terms of divergence and vorticity, which are defined as:

$$\hat{\delta_0} := \frac{\partial \hat{u_0}}{\partial \hat{x}} + \frac{\partial \hat{v_0}}{\partial \hat{y}}, \quad \hat{\delta_1} := \frac{\partial \hat{u_1}}{\partial \hat{x}} + \frac{\partial \hat{v_1}}{\partial \hat{y}}, \quad \cdots \tag{23}$$

$$\hat{\zeta_0} := \frac{\partial \hat{v_0}}{\partial \hat{x}} - \frac{\partial \hat{u_0}}{\partial \hat{y}}, \quad \hat{\zeta_1} := \frac{\partial \hat{v_1}}{\partial \hat{x}} - \frac{\partial \hat{u_1}}{\partial \hat{y}}, \quad \cdots \tag{24}$$

and denoting the Lagrangian derivative along geostrophic winds as $D_0/D\hat{t}$, we obtain a set of equations[3] for $\hat{\zeta_0}$, $\hat{\delta_1}$, and $\hat{\eta}_0$:

$$\begin{cases} \dfrac{D_0 \hat{\zeta_0}}{D\hat{t}} + \hat{\delta_1} + \hat{\beta} \dfrac{\partial \hat{\eta}_0}{\partial \hat{x}} = 0 & \text{(27a)} \\ \dfrac{D_0 \hat{\eta}_0}{D\hat{t}} + \hat{\delta_1} = \dfrac{\mathrm{Da}}{\mathrm{Ro}} \hat{j}_0 & \text{(27b)} \\ \hat{\zeta_0} = \hat{\nabla}^2 \hat{\eta}_0 & \text{(27c)} \end{cases}$$

---

[3] Taking the derivative of equation (22b) with respect to $\hat{x}$ and subtracting the derivative of equation (22a) with respect to $\hat{y}$, we obtain:

$$\frac{\partial}{\partial \hat{x}} \left(\frac{\partial \hat{v_0}}{\partial \hat{t}} \right) - \frac{\partial}{\partial \hat{y}} \left(\frac{\partial \hat{u_0}}{\partial \hat{t}} \right) + \frac{\partial}{\partial \hat{x}} (\hat{\vec{u_0}} \cdot \hat{\vec{\nabla}} \hat{v_0}) - \frac{\partial}{\partial \hat{y}} (\hat{\vec{u_0}} \cdot \hat{\vec{\nabla}} \hat{u_0}) + \frac{\partial \hat{u_1}}{\partial \hat{x}} + \hat{\beta} \hat{y} \frac{\partial \hat{u_0}}{\partial \hat{x}} + \frac{\partial \hat{v_1}}{\partial \hat{y}} + \hat{\beta} \hat{y} \frac{\partial \hat{v_0}}{\partial \hat{y}} + \hat{\beta} \hat{v_0} = 0 \tag{25}$$

The nonlinear terms $\frac{\partial}{\partial \hat{x}} (\hat{\vec{u_0}} \cdot \hat{\vec{\nabla}} \hat{v_0}) - \frac{\partial}{\partial \hat{y}} (\hat{\vec{u_0}} \cdot \hat{\vec{\nabla}} \hat{u_0})$ can be rewritten using vector identities as $\hat{\vec{u_0}} \cdot \hat{\vec{\nabla}} \hat{\zeta_0} + \hat{\delta_0} \hat{\zeta_0}$, giving:

$$\frac{\partial \hat{\zeta_0}}{\partial \hat{t}} + \hat{\vec{u_0}} \cdot \hat{\vec{\nabla}} \hat{\zeta_0} + \hat{\delta_0} \hat{\zeta_0} + \hat{\delta_1} + \hat{\beta} \hat{y} \hat{\delta_0} + \hat{\beta} \hat{v_0} = 0 \tag{26}$$

Substituting $\hat{\delta_0} = 0$ into equation (26) and equation (22c), we obtain equations (27a) and (27b), respectively. Furthermore, from equations (21a) and (21b), we obtain equation (27c).

Note that, from equation (21c), we have $\hat{\delta}_0 = 0$. Since the solution of the quasi-geostrophic system generally has $\hat{\delta}_1 \neq 0$, the divergence scales as $\{\delta\} \sim \mathrm{Ro}U/L$.

If we neglect quantities higher than the leading order in Rossby number according to:

$$\hat{\zeta} \simeq \hat{\zeta}_0, \quad \hat{\eta} \simeq \hat{\eta}_0, \quad \hat{\delta} \simeq \mathrm{Ro}\hat{\delta}_1, \quad \frac{D}{D\hat{t}} \simeq \frac{D_0}{D\hat{t}}, \quad \hat{j} \simeq \hat{j}_0 \tag{28}$$

we obtain:

$$\begin{cases} \mathrm{Ro}\dfrac{D\hat{\zeta}}{D\hat{t}} + \hat{\delta} + \mathrm{Ro}\hat{\beta}\dfrac{\partial\hat{\eta}}{\partial\hat{x}} = 0 & \text{(29a)} \\ \hat{\delta} = -\mathrm{Ro}\dfrac{D\hat{\eta}}{D\hat{t}} + \mathrm{Da}\hat{j} & \text{(29b)} \\ \hat{\zeta} = \hat{\nabla}^2\hat{\eta} & \text{(29c)} \end{cases}$$

or dimensionally,

$$\begin{cases} \dfrac{D\zeta}{Dt} + \delta + \dfrac{\beta g}{f_0}\dfrac{\partial\eta}{\partial x} = 0 & \text{(30a)} \\ \delta = -\dfrac{1}{H}\dfrac{D\eta}{Dt} + \dfrac{j}{gH} & \text{(30b)} \\ \zeta = \dfrac{g}{f_0}\nabla^2\eta & \text{(30c)} \end{cases}$$

This is the quasi-geostrophic system with diabatic heating.

Derivation of the WTG and QGPV conservation systems based on $\mathscr{T}/\mathscr{M}$

Combining the nondimensional parameters appearing in equation (29b):

$$\frac{\mathrm{Da}}{\mathrm{Ro}} = \frac{JL/gHU}{U/fL} = \frac{J}{fU^2}\cdot\frac{f^2L^2}{gH} = \frac{J}{fU^2}\cdot\frac{L^2}{L_\mathrm{R}^2} \sim \mathscr{T}/\mathscr{M} \tag{31}$$

Therefore, in this shallow-water system:

$$\begin{cases} \mathscr{T}/\mathscr{M} \to \infty \iff \mathrm{Da} \gg \mathrm{Ro} & \text{(32a)} \\ \mathscr{T}/\mathscr{M} \to 0 \iff \mathrm{Da} \ll \mathrm{Ro} & \text{(32b)} \end{cases}$$

When $\mathscr{T}/\mathscr{M} \to \infty$ (with Da $\gg$ Ro), setting Da $\gg$ Ro in equation (29b), we obtain the following WTG system:

$$\begin{cases} \dfrac{D\zeta}{Dt} + \dfrac{\beta g}{f_0}\dfrac{\partial \eta}{\partial x} = -\dfrac{f_0}{gH} j & \text{(33a)} \\ \delta = \dfrac{j}{gH} & \text{(33b)} \\ \zeta = \dfrac{g}{f_0}\nabla^2 \eta & \text{(33c)} \end{cases}$$

Here, the first equation represents "conservation of absolute vorticity," the second equation represents "balance between divergence and heating," and the third equation represents "geostrophic balance." Geostrophic balance holds widely in the WTG system except very close to the equator where the Rossby number becomes large (Supplementary Fig. 2). As is evident from these equations, in the WTG system, there is no distinction between potential vorticity and absolute vorticity.

Next, when $\mathscr{T}/\mathscr{M} \to 0$ (with Da $\ll$ Ro), setting Da $\ll$ Ro in equation (29b), we obtain the following QGPV conservation system:

$$\begin{cases} \dfrac{D\zeta}{Dt} + \dfrac{\beta g}{f_0}\dfrac{\partial \eta}{\partial x} - \dfrac{f_0}{H}\dfrac{D\eta}{Dt} = 0 & \text{(34a)} \\ \delta = -\dfrac{1}{H}\dfrac{D\eta}{Dt} & \text{(34b)} \\ \zeta = \dfrac{g}{f_0}\nabla^2 \eta & \text{(34c)} \end{cases}$$

Here, the first equation represents "quasi-geostrophic potential vorticity conservation," the second equation represents "continuity equation," and the third equation represents "geostrophic balance." In the QGPV conservation system, the mechanical source dominates over the thermal source as a driving force, so the QGPV defined on the left-hand side of the first equation is conserved. Divergence (i.e., vertical motion) is then determined diagnostically from the continuity equation (second equation) in a way that satisfies QGPV conservation.

From these results, it is shown that $\mathscr{T}/\mathscr{M}$ is the parameter determining the "phase transition" between the WTG system and the QGPV conservation system, which are known to dominate in the tropics and in the midlatitudes, respectively. Combined with the results of the previous section, it is shown that two interior regions with different reasons for existence, i.e., the WTG atmosphere ($\mathscr{T}/\mathscr{M} \to \infty$) and the QGPV conservation atmosphere ($\mathscr{T}/\mathscr{M} \to 0$), are smoothly connected at a "boundary layer" where $\mathscr{T}/\mathscr{M} \sim 10$, that is, near latitude $\phi_{TM} \simeq 19^\circ$.

Supplementary Figures

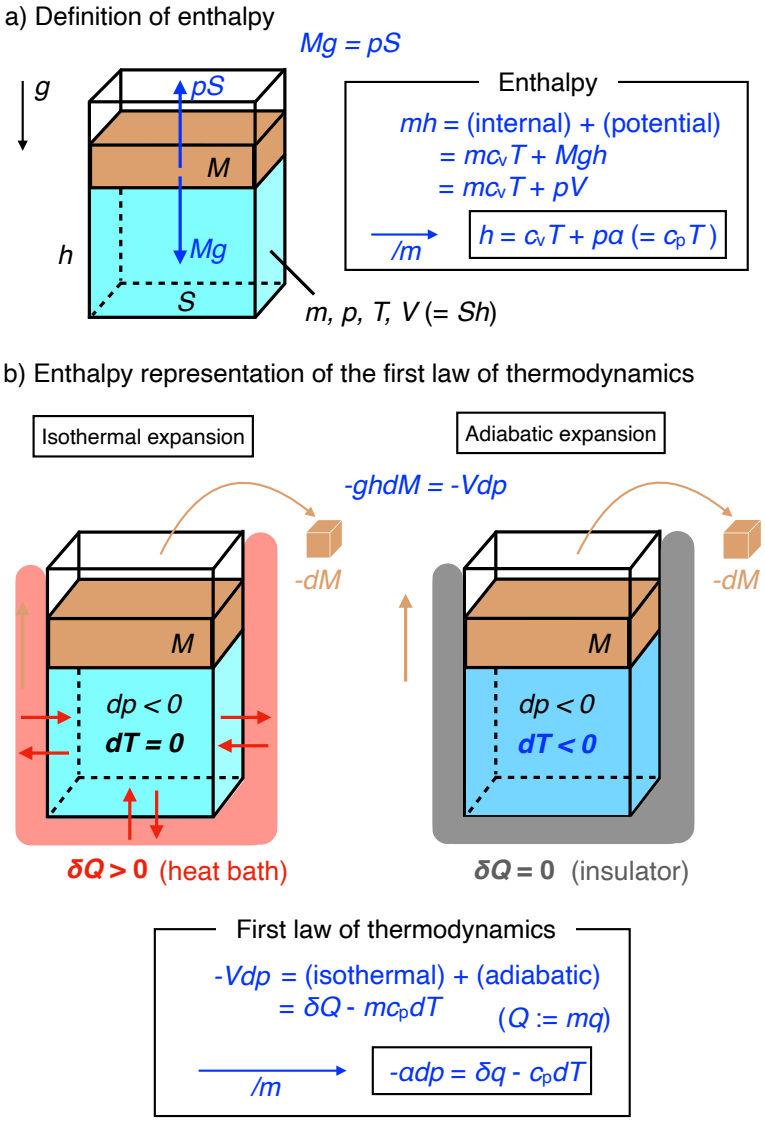

FIG. 1. **Enthalpy and its representation of the energy conservation.** (a) Schematic explaining the definition of enthalpy using a system that consists of a container, a piston, and air. (b) Schematic showing the two possible processes (i.e., isothermal and adiabatic expansions) to decrease air pressure, explaining the enthalpy representation of the first law of thermodynamics.

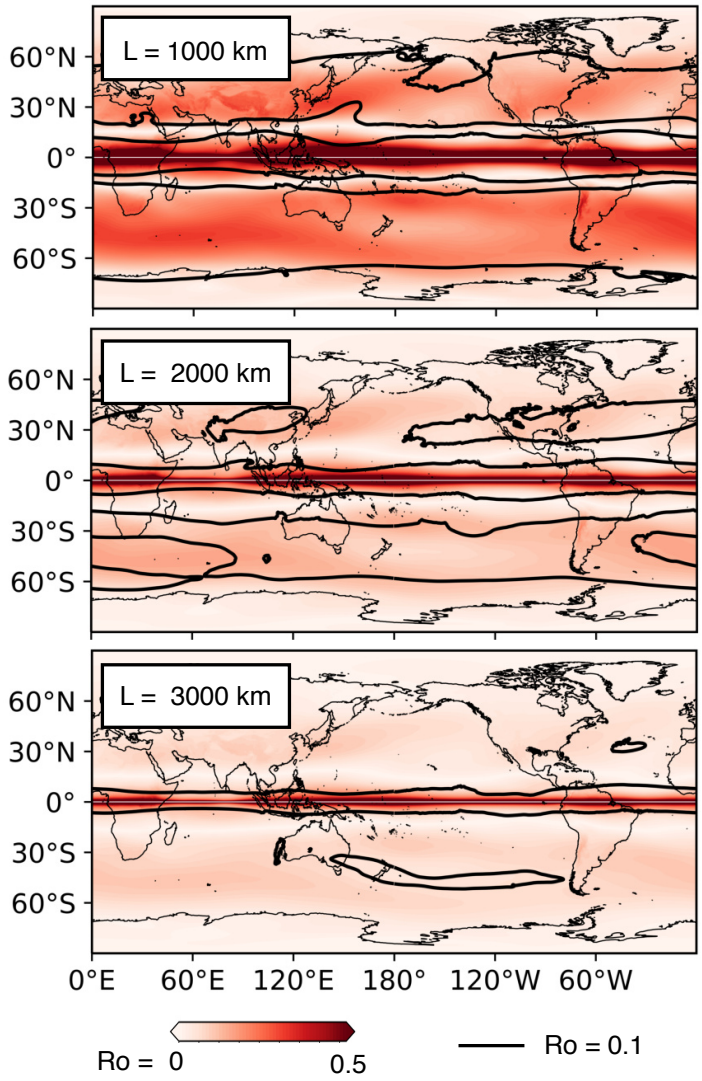

FIG. 2. **Spatial distribution of the Rossby number.** Annual-mean Rossby number in 2024 calculated as U/fL, where U is the mass-weighted vertical-mean wind (*see* Methods), f is Coriolis parameter, and L is the horizontal scale.

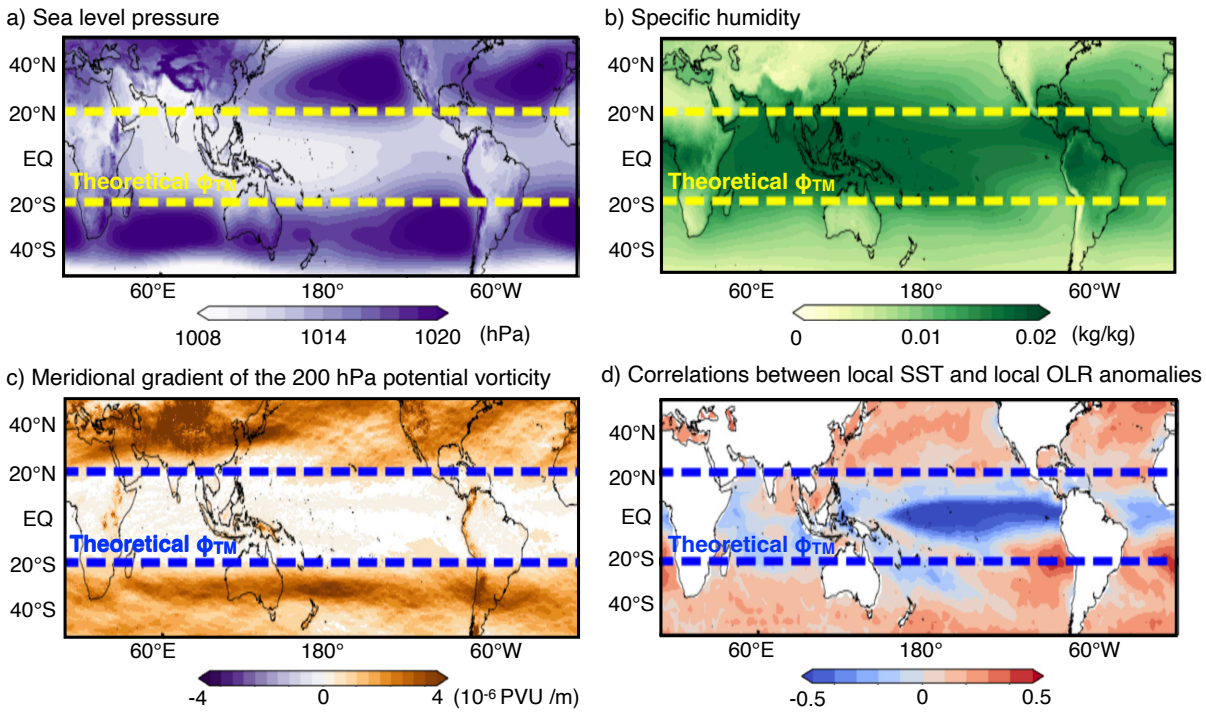

FIG. 3. **Implications of the T/M theory for various meteorological variables.** (a) Annual-mean sea level pressure in 2024. (b) Annual-mean specific humidity at 500 hPa in 2024. (c) Annual-mean meridional potential vorticity gradient at 200 hPa in 2024. 1 PVU = 10^{-6} (K·m^2)/(kg·s). (d) Correlation coefficients between local SST and local outgoing longwave radiation calculated for 1982-2024 at each 2.5-degree global grid.

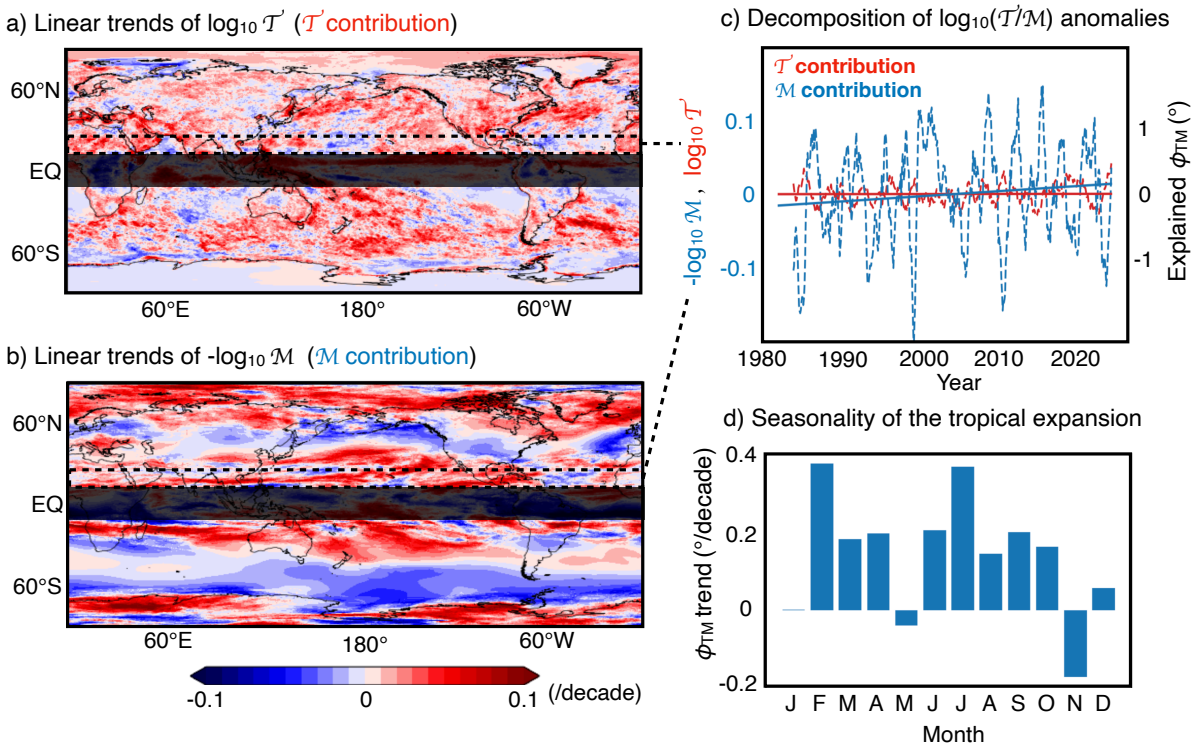

FIG. 4. **Analysis on the "global tropicalization" and its associated tropical expansion.** (a) Top, As in Fig. 4a, but for $\log_{10}\mathscr{T}$. Bottom, As in Fig. 4a, but for $-\log_{10}\mathscr{M}$. (b) As in the blue dashed curve in Fig. 4b, but for $\log_{10}\mathscr{T}$ (red) and $-\log_{10}\mathscr{M}$ (blue). (d) Seasonal variability of zonal-mean ϕ_{TM} trends in the Northern Hemisphere.

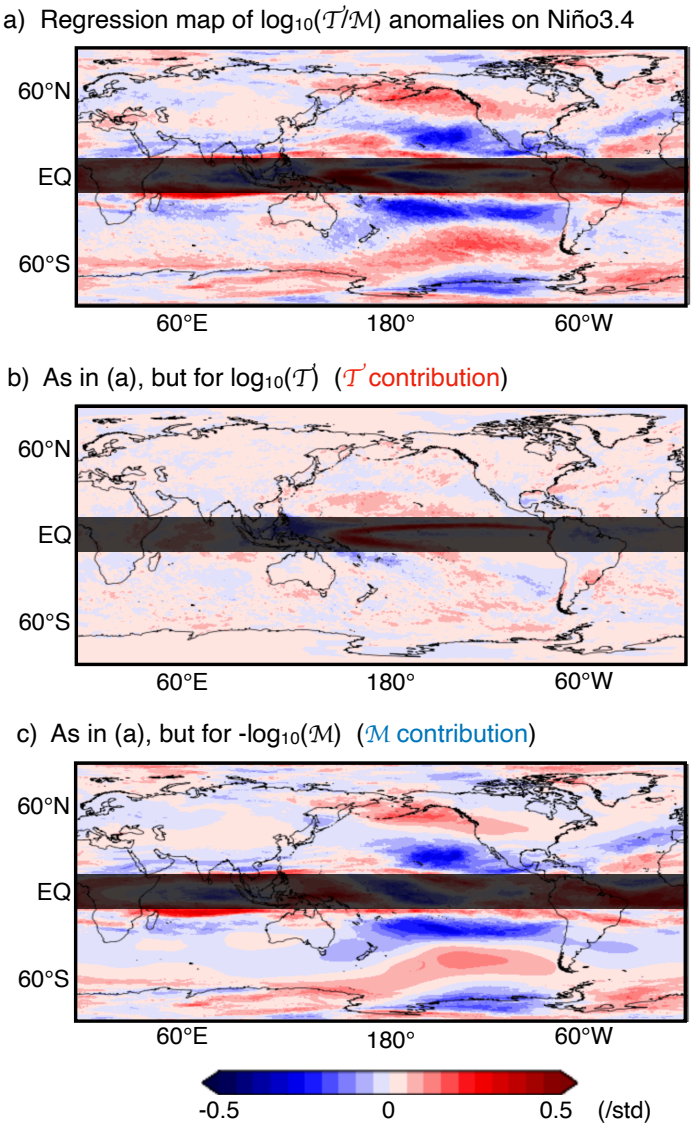

228 FIG. 5. **The T/M response to ENSO.** (a) Regression map of $\log_{10} \mathscr{T} / \mathscr{M}$ onto the Niño 3.4 index (blue curve
229 in Fig. 4d). (b) As in (a), but for $\log_{10} \mathscr{T}$. (c) As in (a), but for $-\log_{10} \mathscr{M}$.